

# Measuring Scars of Periodic Orbits

L. Kaplan\*

Department of Physics and Society of Fellows,  
Harvard University, Cambridge, MA 02138

E. J. Heller†

Department of Physics and Harvard-Smithsonian Center for  
Astrophysics, Harvard University, Cambridge, MA 02138

The phenomenon of periodic orbit scarring of eigenstates of classically chaotic systems is attracting increasing attention. Scarring is one of the most important “corrections” to the ideal random eigenstates suggested by random matrix theory. This paper discusses measures of scars and in so doing also tries to clarify the concepts and effects of eigenfunction scarring. We propose a new, universal scar measure which takes into account an entire periodic orbit and the linearized dynamics in its vicinity. This measure is tuned to pick out those structures which are induced in quantum eigenstates by unstable periodic orbits and their manifolds. It gives enhanced scarring strength as measured by eigenstate overlaps and inverse participation ratios, especially for longer orbits. We also discuss off-resonance scars which appear naturally on either side of an unstable periodic orbit.

## I. INTRODUCTION

### A. Background

The modern field of quantum chaology often associates classically chaotic motion on the one hand with aspects of random matrix theory (RMT) on the other [1]. These aspects include level repulsion in the quantum spectrum as given by the appropriate random matrix ensemble, Gaussian random wavefunctions with Bessel correlations, etc. Since Hamiltonian dynamics cannot be truly random, numerous recent contributions to the field address the many sorts of “corrections” to the random matrix approximation. One of those corrections is the phenomenon of scarring of quantum eigenstates by *isolated* unstable periodic orbits of the corresponding classical system [2].

In the early 1980’s MacDonald in unpublished work [3] found clear evidence of non-isolated marginally unstable periodic orbits in certain stadium eigenstates (which he named the “bouncing ball” states). He also tentatively noted the possible influence of an *isolated, unstable* periodic orbit on a few of the calculated eigenstates, but gave no further attention to this effect. In the subsequent

first published account of numerically computed stadium eigenstates by MacDonald and Kaufman [4] (which to the authors’ knowledge contains the first eigenstates reported for any completely chaotic system), attention was focussed not on periodic orbit effects but on the nodal structure of the eigenstates. The conclusion was that the expected pattern of nodal lines for random eigenstates had been reached. This early work also noted broad agreement with the Bessel function form of the eigenstate spatial self-correlation function for chaotic billiards, as first discussed and predicted by Berry [5]. The paper [4] appeared during the first epoch of quantum chaos theory, when much excitement was being generated by noting similarities between computed eigenstate properties of classically chaotic Hamiltonian systems and RMT [1].

Stronger numerical evidence for the influence of individual periodic orbits on eigenstates, together with a theoretical explanation for scarring in a chaotic system, was introduced in 1984 [2]. Loosely speaking, a scar is a concentration of extra and unexpected (as compared to the RMT prediction) eigenstate density near an unstable classical periodic orbit. This extra concentration has no classical analogue, which puts scarring into the family of quantum localization effects. A semiclassical theory for the existence and strength of scars was given, using time domain arguments and dynamics linearized around the periodic orbits. This theory has seen a number of extensions and applications, including Bogomolny’s coordinate space theory of scarring [6] and Berry’s Wigner phase space theory [7]. (The 1984 paper [2] had been essentially a Husimi phase space, or Gaussian wavepacket, theory.) All these theories were based on the linearized dynamics in the vicinity of a periodic orbit, but there were important differences. For example, an essential ingredient to the strength of scarring, the Lyapunov stability exponent of the periodic orbit, enters only in the wavepacket approach [2], while the important observation of “knots” of high density at self-conjugate (focal) points in coordinate space along the orbit was made by Bogomolny [6].

Scarring has been shown to affect physical systems of various sorts [8] and even the performance of devices such as a tunnel diode [9]. Recently one of us showed that the decay of metastable states can be strongly affected by scarring, in that highly anomalous lifetime distributions are possible depending on where decay channels are located with respect to the shortest periodic orbits of the

---

\*kaplan@physics.harvard.edu

†heller@physics.harvard.edu

system [10].

The following litany of properties of eigenfunction scarring has led to some confusion and to several attempts at developing quantitative measures of this phenomenon: (1) The manifestations of scarring can be subtle or obvious. (2) Measures of scarring can be basis dependent. (3) Scar-like structures are found to occur even in artificially constructed purely random wavefunctions [11]. (4) Statistical fluctuations allowed by RMT might account for some apparently scarred states.

Recent work in our laboratory [12–14] has focussed much attention on quantifying the phenomenon of scarring, confirming the role of the instability exponent of a given periodic orbit, and further examining the consequences of these findings, including experimental issues and the effects of antiscars. Related work of ours has noted that scarring is concordant with bounds on the ergodicity of eigenstates as developed by Schnirelman [15], Zelditch [16], and Colin de Verdiere [17]. A review of recent developments in the theory of scarring was recently written by one of the authors [14]. The present work completes an important part of the picture by explicitly addressing the basis dependence of measures of scarring and arriving at a universal and optimal basis for measuring scars, while not diminishing the utility of simpler and more *ad hoc* measures.

## B. Measures

If eigenstates were ideal random matrix states, then all probe states would be equivalent, in that Gaussian random statistics in one basis guarantees Gaussian random statistics in every other. In the RMT literature, it is sometimes noted that for any given member of the ensemble there will be a diagonalizing basis; however, this basis is non-generic and is itself randomly varying from one member of the ensemble to another. One way of approaching the corrections to RMT in Hamiltonian systems with a classical analogue is to show that there exist special bases which are nonrandom and which come from deterministic dynamical evolution. These special bases bring the Hamiltonian into a manifestly non-RMT form. *Any* basis which systematically shows non-RMT wavefunction statistics for a classically chaotic system is thus potentially significant. Seen in this light, the basis dependence of scar measures should be expected and even exploited.

One such special basis is that of complex Gaussian wavepackets. Complex Gaussians have adjustable position and momentum expectation values, and satisfy minimum uncertainty conditions in some system of axes in phase space, making them excellent measuring devices for the structure of eigenstates in phase space. This basis was the one chosen in [2]. For Gaussians centered on periodic orbits, asymptotically exact ( $\hbar \rightarrow 0$ ) semiclassical dynamics for a fixed short time places rigorous non-RMT

constraints on the statistics of eigenstate projections onto the Gaussian. Some of the eigenstates (precisely which ones cannot be specified in this short-time theory) are then required to have large projections onto the periodic orbit centered Gaussian (these are the scarred states), while many more are shown to have anomalously *small* projections (the anti-scarred states). We review why this is so in the next section. The inverse participation ratio (IPR) of such orbit-centered Gaussian packets is anomalous, and is governed by the classical Lyapunov stability exponent  $\lambda$  as

$$\text{IPR} \sim \frac{1}{\lambda} \quad (1)$$

for small  $\lambda$ . (Note that  $\hbar$  does not appear in this scaling, implying survival of the scarring phenomenon into the classical limit.) Some individual eigenstate projections onto the Gaussian basis were shown to be enhanced by at least  $\frac{1}{\lambda}$  over the RMT expectation [2] (again, exactly which ones is not known and would require much longer time information). It is sometimes stated that scar theory is not a theory of individual eigenstates. While that is true in many respects, especially of the energy averaged approaches such as Bogomolny’s [6], the Husimi (Gaussian packet) phase space theory of scars [2] predicts there must exist individual scarred states, especially for small instability exponent  $\lambda$ .

As versatile as the Gaussian basis is, there are choices to be made and certain optimizations possible which further sensitize the probe basis to the structures which classical dynamics imprints onto the eigenstates of classically chaotic systems. Before discussing this further, we note a *reductio ad absurdum* which places restrictions on how far the refinement of scarring measures can go. Some years ago, Tomsovic and Heller [18] were successful in constructing a high quality scarred eigenstate of the stadium billiard using only semiclassical methods (the overlap of the semiclassical state with the exact eigenstate being 0.87). Using such near-eigenstates as a probe basis would lead to extreme non-RMT behavior in which all but one eigenstate have small projection onto the test state. Furthermore, including large parts of the classical invariant manifolds leading far from the region of a given periodic orbit subverts the idea of a scar of a periodic orbit.

Fortunately there is a quite natural stopping point in the construction of a test basis: we use only the linearized dynamics (tangent map) near any given periodic orbit in constructing measures of scarring. In this way we arrive at test states that are understandable in terms of simple invariant manifold structures of classical phase space near periodic orbits. Although the test states can be more complicated than a single Gaussian, these more sophisticated test states are still determined by short time linear dynamics (of order of the time over which the dynamics is linearizable, which scales as  $|\log \hbar|/\lambda$ ). (Recall that a given orbit can be highly nonlinear, yet possess a linearizable tangent map in its vicinity.)

In constructing linear scar measures we still have a number of choices to make:

- What is the uncertainty zone of the test state in phase space (in the case of a Gaussian, this is the uncertainty ellipse in phase space). Scar measures will change for example depending on whether the ellipse lies along the stable or unstable manifolds of the orbit or away from them.
- For a given period-one periodic orbit, do we construct a test state with a Gaussian placed at one point along the orbit or do we construct a tube (closely spaced Gaussians on the orbit) of some sort, and is this tube to be a coherent superposition of the Gaussians or an incoherent one? (In the case of a discrete-time map, this corresponds to placing a Gaussian at each periodic point of a periodic orbit with length greater than one.)
- Should we take coherent linear combinations of a given Gaussian and its pre- and post-images, producing a new test state consisting of several different Gaussians at each point along the orbit? (This idea leads to the “universal” measure of scarring.)

### C. Brief history of scar measures

There are several threads in the attempt to make good measures of scarring. The original approach [2] amounted to projection onto single Gaussians (the Husimi measure); an  $O(1/\lambda)$  enhancement in the infinite-time average return probability for a Gaussian placed on an unstable periodic orbit was noted for small  $\lambda$ . This implies that some eigenstates in specified energy ranges are systematically enhanced by  $O(1/\lambda)$  in the periodic orbit regions over the RMT predictions. Much later it was realized that this local enhancement has a dramatic effect on the tails of the  $|\psi|^2$  distribution [13].

Any theory of scarring implies some measure of the effect. The first theory of wavefunction scarring in position space was developed by Bogomolny [6]. Bogomolny smoothed the wavefunction intensity over some small energy range  $\Delta E$  using the semiclassical Green’s function; scars are represented as smoothed sums over effectively finitely many periodic trajectories of the system. Bogomolny’s semiclassical Green’s function approach is very closely related to our wavepacket dynamics method, as the semiclassical Green’s function can be obtained from the semiclassical time-domain propagator by a stationary-phase Fourier transform. One difference between the approaches is that Bogomolny envisions summing over a large number of periodic orbits to get as close as possible to an energy domain resolution of order of a mean level spacing. As mentioned above, in some systems it is indeed possible to use semiclassical methods to compute individual eigenstates of the system [19]. In fact for this purpose one needs information only about orbits

of period up to the mixing time (which scales logarithmically with  $\hbar$ ) rather than the Heisenberg time (which scales as a power law). However, our aim here is to make predictions about the distribution of scarring strengths based only on linearized information around *one* periodic orbit; for this purpose most other orbits which produce additional oscillations in the density of states may be treated statistically [20]. It is important to note in this context that if we are measuring wavefunction intensities on a given short classical periodic orbit  $\mathcal{P}$ , then in the semiclassical limit there are no other short orbits that come close to this orbit (on a scale of  $\hbar$ ) in phase space. The only oscillatory contributions which will need to be taken into account are from orbits closely related to orbits *homoclinic* to  $\mathcal{P}$  [homoclinic orbits are those that approach  $\mathcal{P}$  at large negative times, perform an excursion away from  $\mathcal{P}$  into other regions of phase space, and then again approach  $\mathcal{P}$  at large positive times]. In fact, in the  $\hbar \rightarrow 0$  limit the periodic orbit sum for a point  $x$  on a given periodic orbit  $\mathcal{P}$  can be written equivalently as a contribution from the orbit  $\mathcal{P}$  itself plus a sum over trajectories homoclinic to  $\mathcal{P}$ . Although the two points of view (periodic and homoclinic sum) are mathematically equivalent, the homoclinic sum approach makes explicit the special role of the orbit  $\mathcal{P}$  near which we are making measurements. In the homoclinic return formalism, it is also straightforward to see that the long-time recurrences of a wavepacket launched at  $x$  are correlated and enhanced in a way that is determined entirely by the stability matrix of the short orbit  $\mathcal{P}$ .

A position space basis, though obviously physically natural in many measurement situations, is not generally an optimal one for detecting scar effects. Unless the periodic point  $x$  happens also to be a focusing point of classical trajectories near the orbit, only a small fraction of the total scar strength is captured in the position basis, and the fraction becomes smaller as  $\hbar$  decreases (or as the energy increases). An easy way to see this is to notice that the effects of a classical trajectory in quantum mechanics *generically* extend to a region around the orbit scaling not as a wavelength but rather as the square root of a wavelength (and similarly the affected region scales as the square root of the total number of channels in momentum space). Thus, unless either the stable or unstable manifold of the orbit  $\mathcal{P}$  at periodic point  $x$  happens to be oriented along the momentum direction, the position space basis will not be optimal, as reflected in the falling off of the focusing prefactor with energy in the semiclassical Green’s function (and similarly the momentum basis will not be optimal, unless one of the two invariant manifolds is oriented along the position direction). All this will become more clear in the exposition of the following section. In any case, one should keep in mind that a position space basis can always be considered as a special limiting case of the Gaussian wavepacket test state, where the position uncertainty of the wavepacket becomes comparable to a wavelength, and the momentum uncertainty becomes large.

A Wigner phase space analysis of the scarring phenomenon was given by Berry [7]. Berry considered the Wigner function, again smoothed over an energy interval  $\Delta E$  near  $E$ . Being formulated in phase space, the approach more closely resembles that of [2]. Working in Wigner phase space instead of Husimi space also eliminates the need to choose the (apparently arbitrary) eccentricity and orientation of the Gaussian wavepackets. The downside of Wigner phase space is the absence of a positivity condition on the Wigner distribution; thus the value of the spectral function cannot be considered as corresponding to an intensity or a probability of being found near a certain point  $x$  (and random matrix theory is therefore not applicable). The Husimi function, which is manifestly positive definite, is identically a phase space smoothing of the Wigner distribution over a phase space region scaling as  $\hbar$ . The ambiguity in choosing the Gaussian centered on  $x$  over which this smoothing is to be performed is indeed an important issue, to be considered carefully in the following. We will see that to obtain the *maximal* scarring effect, the Gaussian must be chosen to be properly oriented along the stable and unstable directions at the periodic point. [An arbitrarily large wavepacket width is allowed along either of these directions, with a correspondingly small width in the orthogonal direction. Also, strong, but non-maximal, scarring will generally be obtained for any wavepacket with width scaling as  $\sqrt{\hbar}$  in both the position and momentum directions.]

A common limitation of the analyses [2,6,7] is that they make no prediction about the properties of the spectral fluctuations on scales much smaller than  $\hbar/T_D$ , where  $T_D \sim T_P/\lambda$  is the decay time of the unstable orbit with period  $T_P$ . Therefore it is not possible to make quantitative predictions about *specific* individual wavefunction intensities, participation ratios, etc., without explicitly doing a Gutzwiller sum over *all* periodic orbits. Even if the sum can be performed, it is by no means clear that it will converge in all cases (e.g. in systems where caustics are important [21]). When the sum does converge it may produce individual semiclassical wavefunctions very different from the quantum eigenstates, due to diffraction and other “hard quantum” effects. Furthermore, such Heisenberg-time calculations are extremely sensitive to small perturbations on the system. What one would like is to be able to say precisely how often a given single-wavefunction scar strength will appear on a given orbit, at what energy, and at what parameter values. In the semiclassical limit, this can in fact be done using only information about linearized dynamics near the orbit itself, and, in some cases, about a few strong isolated homoclinic recurrences which cannot be treated statistically.

Agam and Fishman [22] define the weight of a scar by integrating the Wigner function over a narrow tube in phase space, of cross-section  $\hbar$ , surrounding the periodic orbit. Li and Hu integrate over coordinate space tubes [23]. Alternatively, de Polavieja, Borondo, and Benito [24] construct a test state highly localized on a

given periodic orbit using short-time quantum dynamics.

Klakow and Smilansky [25] have used a scattering approach to quantization to study the wavefunctions of billiard systems. They treat carefully the wavefunctions on the Poincare surface of section, and relate their properties to scarring in configuration space. Ozorio de Almeida [26] uses the Weyl representation to establish connections between classical and quantum dynamics, with particular application to the semiclassical Wigner function and scars. Tomsovic [27] has used parametric variation as a new method for studying scar effects; scars are shown to induce correlations between wavefunction intensities on a periodic orbit and the level velocities of these wavefunctions when certain system parameters are varied. We also mention the work of Arranz, Borondo, and Benito [28] who have probed the intermediate region between regular and strongly chaotic quantum behavior, and have shown how scarred states first arise from the mixing of pairs of regular wavefunctions as  $\hbar$  is decreased (but well before one reaches the semiclassical limit which is the main focus of the present work). Finally, several groups [29,31] have studied the hyperbolic scar structures associated not only with the periodic orbit itself but with its invariant manifolds and homoclinic orbits.

In the next section we discuss scarring as measured by individual Gaussian wavepackets, which was the basis of [2]. A single localized test state may be optimized to conform to the classical invariant manifolds in the vicinity of a scar. In subsequent sections we go considerably beyond this measure, refining our templates to better detect scarring. In Section III we address the apparent arbitrariness in the choice of a point along the orbit at which to make the measurement, and in the eccentricity of the test Gaussian, and eliminate these ambiguities by building a wavepacket-averaged measure of scarring. Following this, in Section IV, we use coherent linear combinations of the localized test states as a more sensitive measure. In Section V, off-resonance scars living on either side of an unstable periodic orbit are shown to follow naturally from our formalism. In Section VI extensions to higher-period orbits and continuous time are discussed, followed by concluding remarks in Section VII.

## II. GAUSSIAN WAVEPACKET SCARRING

### A. Semiclassical dynamics of a Gaussian wavepacket

We begin with a review of the original (Gaussian wavepacket) theory of scarring, as discussed in detail recently in [12]. In the course of the discussion, the key concepts of the autocorrelation function, the short-time spectral envelope, nonlinear recurrences, and the inverse participation ratio will be introduced. We will also see the inherent limitations of measuring scar strength using single Gaussian test states, pointing the way to the con-

struction of improved “scarmometers”<sup>1</sup> in the following sections.

Consider an arbitrary (unstable) periodic orbit of a chaotic system. For the purpose of simplifying the exposition, and without loss of generality, we take the periodic orbit to be a fixed point of a discrete-time area-preserving map on a two-dimensional phase space. If the periodic orbit in question is in fact a higher-period orbit of such a map, or is an orbit of a continuous-time dynamics in two spatial dimensions, we can reduce the problem to the preceding case by iterating the original map, or by taking a surface of section map, respectively.<sup>2</sup>

We start with a fixed point at the origin of phase space. Furthermore, we can take the stable and unstable directions at the fixed point to be vertical ( $p$ ) and horizontal ( $q$ ), respectively (we can always get the local dynamics into this form by first performing a canonical transformation on the coordinates). Then the only parameter describing the local (linearized) dynamics near the orbit is  $\lambda$ , the instability exponent for one iteration of the orbit. Locally, the equations of motion are given by

$$\begin{aligned} q &\rightarrow q' = e^{\lambda t} q \\ p &\rightarrow p' = e^{-\lambda t} p. \end{aligned} \quad (2)$$

We now turn to the construction of a test state which can be used to measure the intensity of eigenstates near the chosen periodic orbit. An obvious choice is a Gaussian wavepacket centered on the fixed point:

$$a_\sigma(q) = \left( \frac{1}{\pi\sigma^2\hbar} \right)^{1/4} e^{-q^2/2\sigma^2\hbar}. \quad (3)$$

This is a minimum-uncertainty state centered at the origin of phase space, with width  $\sigma\sqrt{\hbar}$  in the  $q$ -direction and  $\sqrt{\hbar}/\sigma$  in the  $p$ -direction.  $\sigma$  is at this stage an arbitrary parameter:  $\sigma^2$  is the aspect ratio of the phase-space Gaussian, typically chosen to be of order unity. Ambiguity in the choice of  $\sigma$  is an important issue that we will return to at the beginning of the next section.

Eigenstate overlaps with our test state will provide a good measure of eigenstate intensities near the periodic orbit; however, we find it useful to begin by working in the time domain (our results will then be applied to eigenstate properties in the following subsection).

For small enough  $\hbar$ , the wavepacket  $|a_\sigma\rangle$  and its short-time iterates are contained well within the linear regime. As long as the wavepacket stays in the phase space region surrounding the periodic orbit in which the linearized equations of motion Eq. 2 apply, the evolution of the wavepacket is completely semiclassical, given simply by

the stretching of the  $q$ -width parameter  $\sigma$ . More explicitly, at short times we have

$$U^t|a_\sigma\rangle \approx U_{\text{lin}}^t|a_\sigma\rangle = e^{-i\phi t}|a_{\sigma e^{\lambda t}}\rangle, \quad (4)$$

where  $U$  is the unitary operator implementing the quantum discrete-time dynamics,  $U_{\text{lin}}$  represents the quantization of the linearized behavior near the periodic orbit, and  $t$  is time, measured in units of a single mapping. Here  $-\phi$  is a phase associated with one iteration of the periodic orbit: it is given by the classical action in units of  $\hbar$ , plus Maslov indices if appropriate.

The autocorrelation function of the wavepacket is defined as the overlap of the evolved wavepacket with itself:

$$A(t) = \langle a_\sigma|U^t|a_\sigma\rangle, \quad (5)$$

which at short times is seen from Eqs. 3, 4 to be

$$A_{\text{lin}}(t) = e^{-i\phi t} \langle a_\sigma|a_{\sigma e^{\lambda t}}\rangle = \frac{e^{-i\phi t}}{\sqrt{\cosh(\lambda t)}}, \quad (6)$$

by performing a simple Gaussian integration. The ‘lin’ subscript indicates that Eq. 6 describes the piece of the autocorrelation function coming from the linearized dynamics around the periodic orbit. For a weakly unstable orbit (small  $\lambda$ ),  $A_{\text{lin}}(t)$  is slowly decaying, with strong recurrences happening for the first  $O(1/\lambda)$  iterations of the orbit. We note that the short-time autocorrelation function  $A_{\text{lin}}(t)$  is  $\sigma$ -independent, a fact that will prove important later on.

At longer times, namely beyond the log time, which scales as

$$T_{\text{log}} \sim \frac{\log fN}{\lambda}, \quad (7)$$

the wavepacket leaves the linearizable region and nonlinear recurrences begin to dominate the return probability. Here  $N$  is the total number of Planck-sized cells in the accessible phase space (also equal to the dimension of the effective quantum mechanical Hilbert space), and  $f$  is the fraction of this phase space (typically  $O(1)$ ) in which the linearized equations of motion (Eq. 2) apply. The nonlinear recurrences correspond to a piece of the wavepacket leaving the linear regime along the unstable manifold, undergoing complicated dynamics far from the periodic orbit, and eventually coming back along the stable manifold to intersect the original wavepacket. Semiclassically, these recurrences are given by a sum over points homoclinic to the original periodic orbit (i.e. points that approach the periodic orbit both as  $t \rightarrow +\infty$  and as  $t \rightarrow -\infty$ ).

Because the long-time homoclinic orbits come back with complicated accumulated phases, and the number of these recurrences grows exponentially with time, one might expect the total long-time return amplitudes to be given by Gaussian random variables. In fact, however, contributions from all homoclinic points lying on a single

<sup>1</sup>The authors thank Eugene Bogomolny for coining this term.

<sup>2</sup>The issue of higher-period orbits and continuous time will be addressed explicitly in Sections III and VI.

homoclinic orbit (i.e. those that are exactly time-iterates of one another) come back in phase with each other, giving rise to short-time correlations in  $A(t)$  for large  $t$  [12]. These correlations are related to the short-time dynamics of the original Gaussian wavepacket. In fact, we can write the return amplitude at times  $T_{\log} \ll t \ll T_H$  ( $T_H = N$  is the Heisenberg time, where individual eigenstates begin to be resolved) as a convolution

$$A(t) = \sum_{\tau} A_{\text{rnd}}(\tau) A_{\text{lin}}(t - \tau). \quad (8)$$

Here  $A_{\text{lin}}$  is the short-time return amplitude, and  $A_{\text{rnd}}$  has the statistical properties of an uncorrelated random Gaussian variable. In effect, random recurrences due to Gaussian fluctuations must have “echoes” that mirror the initial short time decay, since the recurrences re-load the initial state. Also,

$$\begin{aligned} \langle A_{\text{rnd}}(\tau) \rangle &= 0 \\ \langle A_{\text{rnd}}^*(\tau) A_{\text{rnd}}(\tau') \rangle &= \frac{1}{N} \delta_{\tau\tau'}. \end{aligned} \quad (9)$$

The prefactor  $1/N$  provides the proper classical normalization: in the absence of interference effects, the probability to come back is equal to the probability for visiting any other state in the Hilbert space. The average in Eq. 9 is taken over long times  $\tau$ ,  $T_{\log} \ll \tau \ll T_H$ , and/or over an ensemble of systems which all have the same linearized dynamics around our chosen periodic orbit. In either case, the total size of the Hilbert space  $N$  ( $= 1/h$  for a phase space area normalized to unity) has been assumed to be large. We then obtain

$$\begin{aligned} \langle A(t) \rangle &= 0 \\ \langle A^*(t) A(t + \Delta) \rangle &= \frac{1}{N} \sum_s A_{\text{lin}}^*(s) A_{\text{lin}}(s + \Delta). \end{aligned} \quad (10)$$

At times beyond the Heisenberg time, this gets modified [12] to

$$\langle A^*(t) A(t + \Delta) \rangle = \frac{F}{N} \sum_s A_{\text{lin}}^*(s) A_{\text{lin}}(s + \Delta). \quad (11)$$

$F$  is a factor associated with the discreteness of the eigenstates: it is 3 for real eigenstate–test state overlaps and 2 for complex overlaps.

The long-time autocorrelation function is thus self-correlated on a scale  $\Delta \sim \lambda^{-1}$ . Qualitatively, this can be understood on a purely classical level: once probability happens to come back to the vicinity of a weakly unstable periodic orbit, it tends to stay around before leaving again. On the other hand, the overall enhancement in the total return probability at long times:

$$\langle |A(t)|^2 \rangle = \frac{F}{N} \sum_{s=-\infty}^{\infty} \frac{1}{\cosh(\lambda s)}, \quad (12)$$

obtained by combining the general expression Eq. 11 with the short-time overlap dynamics of the Gaussian wavepacket (Eq. 6), is fundamentally an interference phenomenon, and signals a kind of quantum localization, as we shall see next. Note that in the limit  $\lambda \rightarrow 0$  (weak instability) we have

$$\langle |A(t)|^2 \rangle \rightarrow \frac{\pi F}{\lambda N}; \quad (13)$$

i.e. the enhancement factor in the long-time return probability is proportional to  $\lambda^{-1}$  [2].

## B. Local density of states

We now define  $S(E)$  to be the fourier transform of the autocorrelation function,

$$S(E) = \frac{1}{2\pi} \sum_{t=-\infty}^{+\infty} A(t) e^{iEt}. \quad (14)$$

For a non-degenerate spectrum, it is easy to see (by inserting complete sets of eigenstates) that

$$S(E) = \sum_n |\langle n | a_{\sigma} \rangle|^2 \delta(E - E_n), \quad (15)$$

where  $E_n$  are the eigenvalues of the dynamics, and  $|n\rangle$  are the corresponding eigenstates. Thus, we obtain the local density of states at the wavepacket  $|a_{\sigma}\rangle$  by fourier transforming its autocorrelation function  $A(t)$ . Cutting off the sum in Eq. 14 at  $\pm T_{\log}$ , or equivalently by including only linearized dynamics around the periodic orbit, we obtain *the smoothed local density of states*:

$$S_{\text{lin}}(E) = \sum_t A_{\text{lin}}(t) e^{iEt}, \quad (16)$$

an envelope centered at quasienergy  $E = \phi$  (see Eq. 6), of width  $\delta E \sim \lambda$ , and of height  $\sim \lambda^{-1}$  (a factor of  $2\pi$  has been inserted into the definition of  $S_{\text{lin}}$  for future convenience).  $E = \phi$  is the analogue of the EBK quantization condition for integrable systems; here, because of the instability of the orbit, scarred states can live in an energy range of  $O(\lambda)$  around the optimal energy. States with energy more than  $O(\lambda |\log \lambda|)$  away from resonance tend to be *antiscarred* (i.e. they have less than expected intensity at the periodic orbit).

Now long-time (nonlinear) recurrences as in Eq. 8 lead to fluctuations under the short-time envelope in the full spectrum  $S(E)$ . Because these recurrences involve a random variable *convoluted* with the short time dynamics, in the energy domain we obtain random fluctuations *multiplying* the short-time envelope. (It is easy to see physically that the random oscillations must multiply the smooth envelope: if they were merely added to it, the total spectrum would become negative away from the

peak of the envelope.) Finally, at the Heisenberg time  $T_H = N$ , individual states are resolved [12,13], and we see a line spectrum with a height distribution given by

$$I_{na_\sigma} \equiv |\langle n|a_\sigma\rangle|^2 = r_{an} S_{\text{lin}}(E_n), \quad (17)$$

where  $r_{an}$  are random variables (with mean  $\langle r_{an} \rangle = 1/N$ ) drawn from a chi-squared distribution of one degree of freedom (two degrees of freedom for complex  $\langle n|a_\sigma\rangle$ ). Thus, in the end we obtain a random (Porter-Thomas) line spectrum  $S(E)$ , all multiplying the original linear envelope.

Before concluding this review, we mention the notion of an *inverse participation ratio* (IPR), a very useful measure for studying deviations from quantum ergodicity. We define

$$\text{IPR}_{a_\sigma} = N \sum_n I_{na_\sigma}^2 = N \sum_n |\langle n|a_\sigma\rangle|^4. \quad (18)$$

(Note that  $\sum_n I_{na_\sigma} = 1$  by normalization.) Being the first non-trivial moment of the eigenstate intensity ( $I_{na_\sigma}$ ) distribution, the IPR provides a convenient one-number measure of the strength of scarring (or any other kind of deviation from quantum ergodicity). The IPR would be unity for a wavepacket that had equal overlaps with all the eigenstates of the system; the maximum value of  $N$  is reached in the opposite (completely localized regime), when the wavepacket is itself a single eigenstate. Random matrix theory predicts an IPR of  $F$ , the strong quantum ergodicity factor defined above in Eq. 11.

From Eqs. 14, 15 we see that

$$\text{IPR}_{a_\sigma} = \lim_{T \rightarrow \infty} \frac{N}{T} \sum_{t=0}^{T-1} |A(t)|^2; \quad (19)$$

as one might expect, localization is associated with an enhanced return probability at long times. Now from Eq. 12 we see that scar theory predicts an enhancement in the IPR over random matrix theory:

$$\text{IPR}_{a_\sigma} = F \sum_s \frac{1}{\cosh(\lambda s)} \quad (20)$$

$$\rightarrow F \frac{\pi}{\lambda}, \quad (21)$$

where in the last line the limit of small  $\lambda$  has been taken. ( $F$ , as before, is 3 or 2, depending on whether the states are real or complex, respectively.) The IPR thus decomposes into a product of two contributions: the shape of the short-time envelope coming from the linear dynamics around the periodic orbit, and a quantum fluctuation factor  $F$ , as predicted by Porter-Thomas statistics.

### C. Limitations

The analysis of the previous two subsections has been extensively tested in numerical studies [12,13], which

show that the statistical properties of eigenstate overlaps with Gaussian wavepackets can indeed be described by the scar theory. However, there are inherent limitations in this approach. An obvious one is the ambiguity in the choice of wavepacket width  $\sigma$ . A wavepacket of any width can be used (as long as it and its short-time iterates are well-contained in the linearizable region, which condition is always satisfied for small enough  $\hbar$ ), resulting in the same short-time overlaps, and thus in identical smoothed spectra  $S_{\text{lin}}$ . The IPR is also expected to be enhanced by the same factor for each such wavepacket, depending only on the decay exponent of the periodic orbit itself. It seems intuitively clear that a better measure of scarring should be obtainable by appropriately combining information from wavepackets of all different aspect ratios, thus looking at a hyperbolic phase-space region surrounding the stable and unstable manifolds of the periodic point. Such a test state for measuring scars would incorporate knowledge of the full linearized dynamics around the periodic point, not just knowledge about the location of the periodic point itself.

The ambiguity and apparent arbitrariness of the preceding definition of scarring seems even more pronounced in the case of a higher-period orbit of a map, or for a periodic orbit of a continuous-time dynamics. In either of those cases, the analysis above can be performed at *any* periodic point lying on the orbit. Yet it is known from experience that scars tend to live not at one periodic point only but along the entire orbit. Here, also, more information could presumably be gained by looking at the behavior of an eigenstate near *all* points on a periodic orbit instead of one only, thus obtaining a fuller measure of wavefunction scarring.

The preceding ambiguities will, in the following sections, point us towards a *universal* measure of wavefunction scarring (in the regime of small  $\lambda$ , where the effect is expected to be significant), a measure which takes full advantage of the *entire* periodic orbit and the *full linearized dynamics* in the vicinity of this orbit. In the process, we will see how the insights of various earlier contributors to this field [22,30,24,27,29] can be incorporated into the resulting general approach.

## III. WAVEPACKET INTENSITY AVERAGING

### A. Density matrix test states

Consider again the fixed point of a classical area-preserving map, as introduced in Eq. 2. Given the apparent arbitrariness in the choice of wavepacket which came out of our discussion in the previous section, it seems natural to extend our measure of scarring, replacing the pure Gaussian test state with a density matrix which gives weight to Gaussians of all widths:

$$\rho = \mathcal{N} \int dt e^{-t^2/T_0^2} |a_{\sigma e^{\lambda t}}\rangle \langle a_{\sigma e^{\lambda t}}|. \quad (22)$$

We choose the exponent  $\lambda$  to be the instability exponent of the unstable orbit (Eq. 2), but this choice is in fact arbitrary, and  $\lambda$  can be reabsorbed into the overall normalization factor  $\mathcal{N}$  and the time cutoff  $T_0$ . In the absence of the cutoff  $T_0$ , the hyperbolic test state would be completely scale invariant, giving equal weight to Gaussians of all aspect ratios, from tall and thin to short and wide. The cutoff is, however, necessary because the linearized dynamics of Eq. 2 is in fact only valid in a finite classical region around the periodic orbit (and it also eliminates possible normalization difficulties). We note that Eq. 22 is an *incoherent* superposition of wavepackets of different width, designed to give an unbiased measure of a scar (where the arbitrariness of a given choice of  $\sigma$  is removed).

Let the classical region in which the dynamics is linearizable be given by a square in phase space, with area  $A$  (the exact shape and area are not important, as we will soon see). Then choosing  $\sigma = 1$ , we see that the evolved width  $\sigma\sqrt{\hbar}e^{\lambda t}$  reaches the edge of the linearizable region at time

$$T_0 = \frac{1}{2\lambda} \log \frac{A}{4\hbar}. \quad (23)$$

(Up to constants,  $T_0$  is the same as the log time discussed above in Eq. 7.) We see that a factor of order one ambiguity in the definition of the region  $A$  will lead only to an additive ambiguity in the cutoff time  $T_0$ , irrelevant in the semiclassical limit  $A \gg \hbar$ . Of course the condition that the Gaussian just touching the boundary should be suppressed by a factor of  $1/e$  (as opposed to  $1/e^2$ ,  $1/e^3$ , etc.) is still somewhat arbitrary, leading us to the more general form

$$T_0 = \frac{c}{2\lambda} \log \frac{A}{4\hbar}, \quad (24)$$

where  $c$  is now an arbitrary constant of order unity. In any case, the ambiguity we previously had in the choice of  $\sigma$  (which could be anywhere from  $\sqrt{\hbar}$  to  $1/\sqrt{\hbar}$ , a huge range in the semiclassical regime  $\hbar \ll 1$ ) has now been reduced to a factor of order one constant  $c$  in the definition of  $\rho$ .

In the following section, where we consider *coherent* superpositions of Gaussian wavepackets, we may wish to use a more stringent criterion for the cutoff time  $T_0$ , taking into account the form of the leading nonlinearity of the dynamics near the periodic orbit. Thus, consider the worst-case scenario, where the stable and unstable manifolds both curve quadratically as we move away from the periodic orbit. Then in order for the curvature to be unimportant as the Gaussian stretches along one of the two manifolds, we may require that the distance by which the unstable manifold deviates from the horizontal line at position  $q$  be less than the vertical width (momentum uncertainty) of a state with position width  $q$ . This means  $O(q^2) < \delta p \sim \hbar/q$ , so the maximum distance  $q$  for which this holds scales as  $\hbar^{1/3}$ . Assuming

the same situation obtains along the stable manifold, we obtain that the linearizable area scales as  $\hbar^{2/3}$ , i.e.  $A = A_0^{1/3} \hbar^{2/3}$  for some classically selected area  $A_0$ . Then  $\log(A/\hbar) = \frac{1}{3} \log(A_0/\hbar)$ , i.e. we may take the size of the linearizable region to be the  $\hbar$ -independent value  $A_0$ , provided we also replace  $c \rightarrow c/3$ . Because of the  $O(1)$  ambiguities already present in the choice of  $c$ , we will not dwell here on the numerical values appropriate to various systems. In any case, as we will discuss when subjecting our results to numerical tests in the following section, there is always a tradeoff between larger  $c$  leading to more localization and smaller  $c$  giving more precise agreement with analytical predictions.

Coming back now to Eq. 22, we notice that we could instead have chosen a hard cutoff for the sum over Gaussians, e.g.

$$\rho' = \mathcal{N}' \int_{-T_0}^{T_0} dt |a_{\sigma e^{\lambda t}}\rangle \langle a_{\sigma e^{\lambda t}}|. \quad (25)$$

This would not qualitatively affect our discussion either here or in the following sections (particularly Section IV, where we discuss coherent superpositions of Gaussian test states). The form of Eq. 22, and its extensions which will follow in future sections, is however convenient because it allows for relatively straightforward analytical calculations.

Another important property of Eq. 22 is that  $\rho$  has the same form in momentum space as in configuration space, as can be seen easily by noting that the momentum width  $\sigma_p = \sigma_q^{-1} = \sigma^{-1} e^{-\lambda t}$  and that Eq. 22 is manifestly invariant under  $t \rightarrow -t$ . Thus, the stable and unstable manifolds of the hyperbolic point are treated symmetrically in our definition.

The idea of averaging overlap intensities can of course be extended to resolve another difficulty we encountered at the end of the previous section, namely the apparent ambiguity in treating periodic orbits that are not fixed points. For a period  $T_P$  orbit of a map, we write

$$\rho = \frac{1}{T_P} \sum_{p=0}^{T_P-1} |a_{x_p, \sigma}\rangle \langle a_{x_p, \sigma}|, \quad (26)$$

where  $|a_{x_p, \sigma}\rangle$  is a wavepacket of width  $\sigma$  along the unstable manifold, but centered at periodic point  $x_p$  instead of at the origin. Similarly, for a continuous-time dynamics, we can write

$$\rho = \mathcal{N} \int dx |a_{x, \sigma, \sigma_x}\rangle \langle a_{x, \sigma, \sigma_x}|, \quad (27)$$

where the  $x$  coordinate parametrizes the periodic orbit in phase space, and at each periodic point the wavepacket is chosen to have width  $\sigma_x$  along the direction of the orbit and width  $\sigma$  in the unstable direction at that point on the orbit:

$$a_{x, \sigma, \sigma_x}(x', y') \sim \exp\left[-(x' - x)^2 / \sigma_x^2 \hbar - y'^2 / \sigma^2 \hbar + ip_x(x' - x) / \hbar\right]. \quad (28)$$

Here  $(x, p_x)$  are the position of a phase space point on the periodic orbit and the corresponding momentum, while  $y'$  is a coordinate along the unstable manifold of the orbit at point  $(x, p_x)$ . Eq. 27 has been written down already in Ref. [12], and a connection was made there to the phase-space tubes of Agam, Fishman et al. [22].

Now the orbit averaging of Eqs. 26, 27 can of course be combined with the width averaging introduced in Eq. 22: thus, in the case of a map we may write

$$\rho = \mathcal{N} \sum_{p=0}^{T_P-1} \int dt e^{-t^2/T_0^2} |a_{x_p, \sigma e^{\lambda t}}\rangle \langle a_{x_p, \sigma e^{\lambda t}}|. \quad (29)$$

Here one may legitimately ask why we perform separately the averaging at each periodic point: we could instead have made use of the orbit dynamics and obtained Gaussian wavepackets centered at each of the periodic points starting with one wavepacket only and allowing it to evolve according to the linearized laws of motion. More explicitly, if we take  $|a\rangle$  to be a Gaussian wavepacket of width  $\sigma$  along the unstable direction, centered at periodic point  $x_0$ , we may construct a dynamical density matrix

$$\rho_{\text{dyn}} = \sum_{t=-\infty}^{+\infty} e^{-t^2/T_P^2 T_0^2} |a_{\text{lin}}(t)\rangle \langle a_{\text{lin}}(t)|. \quad (30)$$

Here  $|a_{\text{lin}}(t)\rangle$  is the original Gaussian evolved in accordance with the *linearized* dynamics: for example, if  $t$  is an integer multiple of the period  $T_P$ , then  $|a_{\text{lin}}(t)\rangle$  is centered at the same periodic point as  $|a\rangle$ , but with width  $\sigma e^{\lambda t/T_P}$ .  $T_0$  is defined as before (Eq. 24), using the full instability exponent  $\lambda$  for one iteration of the *entire* primitive orbit.  $\lambda/P$  is the exponent *per time step*; hence the factor of  $T_P^2$  in Eq. 30.

For small  $\lambda$ , where not much stretching has taken place over one period of the orbit, not much difference exists between the averaging methods of Eq. 26 and Eq. 30. We return to this connection between (linearized) dynamics and improved test states in Section IV, where coherent superpositions of Gaussian wavepackets are discussed. Here it suffices to note that because all wavepackets being averaged over in  $\rho_{\text{dyn}}$  are exact time-evolutes of one another (at least in the linear approximation), they all have exactly the same local density of states and inverse participation ratio. In fact this absence of real averaging is there even for the full matrix  $\rho$  of Eqs. 26, 27, 29, in the limit of small  $\lambda$ , as we shall see next.

## B. Measures of scarring from incoherent averaging

Our measure for the strength of scarring for a given eigenstate  $|n\rangle$  is now simply

$$I_{n\rho} \equiv \langle n|\rho|n\rangle. \quad (31)$$

We can construct a wavepacket-averaged local density of states analogous to Eq. 15

$$S_\rho(E) = \sum_n I_{n\rho} \delta(E - E_n), \quad (32)$$

and a corresponding inverse participation ratio

$$\text{IPR}_\rho = N \sum_n I_{n\rho}^2. \quad (33)$$

Notice that  $S_\rho(E)$  is nothing other than a weighted sum of the densities  $S(E)$  of Eq. 15, and thus follows the same linear envelope  $S_{\text{lin}}$  which we have discussed in the previous section. The only thing possibly different about  $S_\rho(E)$  are the oscillations under this envelope. To understand how these oscillations in the averaged local density of states  $\text{IPR}_\rho$  might differ from the Porter-Thomas fluctuations one finds for a single wavepacket, we need to study correlations between local densities of states for different wavepackets centered on the same periodic orbit.

In general, given two wavepackets  $|a\rangle$  and  $|b\rangle$ , we can define a long-time averaged transport probability  $P_{ab}$  [32] as

$$P_{ab} = \lim_{T \rightarrow \infty} \frac{1}{T} \sum_{t=0}^{T-1} |\langle a|U^t|b\rangle|^2. \quad (34)$$

For a nondegenerate spectrum we easily see

$$P_{ab} = \sum_n |\langle a|n\rangle|^2 |\langle b|n\rangle|^2 = \sum_n I_{na} I_{nb}. \quad (35)$$

In particular, the IPR as defined in the preceding section corresponds to the special case  $|a\rangle = |b\rangle$ :

$$\text{IPR}_a = N P_{aa} = N \sum_n I_{na}^2. \quad (36)$$

The  $P_{ab}$  can be thought of as the covariance matrix of the densities of states for different wavepackets, with  $P_{aa}$  being the variances or diagonal matrix elements; the correlation between two densities of states is then given by

$$C_{ab} = \frac{P_{ab}}{\sqrt{P_{aa} P_{bb}}}. \quad (37)$$

We begin with the simplest case, where wavepackets  $|a\rangle$  and  $|b\rangle$  are exact time iterates of one another:  $|b\rangle = |a(t)\rangle$  for some time  $t$ . There, of course  $P_{ab} = P_{aa} = P_{bb}$ , and the correlation is unity (the two local densities of states  $S(E)$  are identical). More explicitly (from Eq. 20) we have in this case

$$P_{ab} = P_{aa} = P_{bb} = \frac{F}{N} g(\lambda), \quad (38)$$

where  $F/N$  is the RMT prediction for the quantum long-time return probability and

$$g(\lambda) = \sum_s |\langle a | U_{\text{lin}}^s | a \rangle|^2 = \sum_s \frac{1}{\cosh(\lambda s)} \quad (39)$$

is a scarring IPR enhancement factor (see Eq. 20). In the last equality the periodic orbit in question has been taken to be period one (a fixed point).

Now consider the opposite extreme case, where wavepackets  $|a\rangle$  and  $|b\rangle$  lie on different periodic orbits of the same classical action (and not related by any symmetry). Then the two local densities of states  $S_a(E)$  and  $S_b(E)$  share the same linear envelope (coming from short time dynamics), but have completely uncorrelated long-time fluctuations:

$$\begin{aligned} I_{na} &= r_{an} S_{\text{lin}}(E_n) \\ I_{nb} &= r_{bn} S_{\text{lin}}(E_n) \end{aligned} \quad (40)$$

with  $r_{an}$ ,  $r_{bn}$  uncorrelated chi-squared variables with mean  $1/N$  (see Eq. 17). Then

$$\begin{aligned} P_{aa} &= P_{bb} = \frac{F}{N} g(\lambda) \\ P_{ab} &= \frac{1}{N} g(\lambda) \\ C_{ab} &= \frac{1}{F}. \end{aligned} \quad (41)$$

The correlation in this case is of order unity but still less than one.

Finally, choose the two wavepackets  $|a\rangle$  and  $|b\rangle$  lying on the same orbit but not exact time-iterates of one another. We can think of wavepacket  $|b\rangle$  as having a part composed of  $|a\rangle$  and its short-time iterates and another part which is statistically independent of  $|a\rangle$  although it lies on the same orbit. The fraction of  $|b\rangle$  which is correlated with  $|a\rangle$  is given by a (normalized) sum of squared overlaps of  $|b\rangle$  with  $|a\rangle$  and its iterates:

$$\frac{\sum_s |\langle b | U_{\text{lin}}^s | a \rangle|^2}{\sum_s |\langle a | U_{\text{lin}}^s | a \rangle|^2} \equiv \frac{g_{ab}(\lambda)}{g(\lambda)}, \quad (42)$$

where Eq. 42 serves as the definition of  $g_{ab}(\lambda)$ . In both numerator and denominator linearized evolution is used, so

$$g_{ab}(\lambda) = \sum_s \frac{1}{\cosh(\lambda(s+z))}, \quad (43)$$

where  $|b\rangle$  is related to some exact time-iterate of  $|a\rangle$  by a stretch of  $e^{\lambda z}$  of the Gaussian along the unstable manifold.

We then have a sum of two contributions:

$$\begin{aligned} P_{ab} &= \frac{F}{N} g(\lambda) \left[ \frac{g_{ab}(\lambda)}{g(\lambda)} \right] + \frac{1}{N} g(\lambda) \left[ 1 - \frac{g_{ab}(\lambda)}{g(\lambda)} \right] \\ &= \frac{F-1}{N} g_{ab}(\lambda) + \frac{1}{N} g(\lambda), \end{aligned} \quad (44)$$

giving

$$C_{ab} = \left[ 1 - \frac{1}{F} \right] \frac{g_{ab}(\lambda)}{g(\lambda)} + \frac{1}{F}. \quad (45)$$

Now as the exponent  $\lambda$  becomes small, *any* optimally oriented wavepacket  $|b\rangle$  lying on the periodic orbit begins to look more and more like an iterate of any other wavepacket  $|a\rangle$ . In that limit,

$$\lim_{\lambda \rightarrow 0} \frac{g_{ab}(\lambda)}{g(\lambda)} = 1, \quad (46)$$

and so the correlation  $C_{ab} \rightarrow 1$ . So the key result is that when scarring is strong ( $\lambda \rightarrow 0$ ), the spectra of all optimal wavepackets centered on the periodic orbit in question are virtually identical, making unnecessary any averaging over width or position along the orbit:

$$\langle n | \rho | n \rangle \rightarrow |\langle a_\sigma | n \rangle|^2, \quad (47)$$

for an arbitrary  $|a_\sigma\rangle$  along the periodic orbit. Therefore, in this limit *any* wavepacket individually provides a universal measure of scarring intensities, obviating the need to construct tubes and other averaging devices.

We now proceed to examine quantitatively the behavior of  $C_{ab}$  in Eq. 45. First, however, we will introduce a model ensemble of systems which will allow us to test numerically this quantitative prediction and others obtained in the following sections.

### C. Ensemble averaging over hard chaotic systems

The classical area-preserving map we will use for our ‘numerical experiments’ is defined on the unit square  $(q, p) \in [0, 1] \times [0, 1]$ , and consists of two parts. The first step is a three-strip generalized baker’s map [31,13] with strip widths  $w_0 + w_1 + w_2 = 1$ . Each vertical strip  $i$  of width  $w_i < 1$  and height 1 is stretched horizontally by a factor of  $1/w_i$  and compressed vertically by a factor of  $w_i$  to make it into a horizontal strip of height  $w_i$  and width 1. The three strips are then stacked on top of each other (left becoming bottom and right becoming top) to reconstruct the unit square. Defining  $s_i = \sum_{j < i} w_j$  to be the left edge of strip  $i$ , we have

$$\begin{aligned} q' &= (q - s_i)/w_i \\ p' &= s_i + p w_i, \end{aligned} \quad (48)$$

where the initial position  $q$  lies in the  $i$ -th strip, i.e.  $s_i \leq q < s_{i+1}$ . The second and final step is a kicked map [33] implemented in the left and right strips of the square, leaving the middle strip undisturbed:

$$\begin{aligned} p'' &= p' - V'_{i'} \left( \frac{q' - s_{i'}}{w_{i'}} \right) \bmod 1 \\ q'' &= s_{i'} + [(q' - s_{i'}) + p'' w_{i'} \bmod w_{i'}]. \end{aligned} \quad (49)$$

Here  $i'$  denotes the number of the strip (0 or 2) containing  $q'$ . The entire mapping Eqs. 48, 49 is now iterated.

The convenience of this two-step model lies in the fact that for any choice of kick potentials  $V_0$  and  $V_2$  acting on the left and right strips, respectively, the middle strip experiences only baker-like horizontal stretching and vertical shrinking. Thus, there is always a fixed point of the system in the middle strip, with coordinates  $q_f = p_f = \frac{w_0}{w_0 + w_2}$ , and stretching exponent  $\lambda = |\log w_1|$ . Furthermore, the stable and unstable manifolds of this fixed point are always locally vertical and horizontal, respectively, consistent with our canonical form Eq. 2. The kicked maps acting on the left and right strips serve to provide parameters which can be easily varied to produce ensemble averaging over the details of the nonlinear long-time recurrences without affecting the local dynamics around the periodic orbit which is being studied.<sup>3</sup> We choose kick potentials

$$V_{0,2}(x) = -\frac{1}{2}x^2 + \frac{K_{0,2}}{(2\pi)^2} \sin 2\pi x, \quad (50)$$

with  $K_{0,2}$  arbitrary parameters. The condition  $|K_{0,2}| < 1$  is sufficient to ensure hard chaos, without regular regions [19]. More general kicking potentials could of course have been used, but we find that the two parameters  $K_{0,2}$  provide a sufficiently large ensemble for our purposes.

The system is quantized in a straightforward and conventional way, by multiplying the unitary matrices implementing baker's map and kicked map dynamics [31,33].

#### D. Numerical tests

We proceed to test the density of states correlations  $C_{ab}$  (Eq. 45) for the fixed point orbit of the map introduced above. The wavepacket  $|a\rangle$  with horizontal width  $\sigma\sqrt{\hbar}$  and vertical width  $\sqrt{\hbar}/\sigma$  is placed on the fixed point. We then define a family of wavepackets  $|b(z)\rangle$  of (horizontal) widths  $\sigma e^{\lambda z}\sqrt{\hbar}$ . Notice that for integer  $z$ ,  $|b(z)\rangle$  is an exact iterate of  $|a\rangle$  (in the linear approximation), and thus in that approximation the densities of states are identical and the correlation  $C_{ab} = 1$ . The differences are expected to be greatest at half-integer  $z$  where  $|b\rangle$  is most unlike any iterate of  $|a\rangle$ . The correlation  $C_{ab}$  is now plotted as a function of  $z$  for  $0 \leq z \leq 1$  in Fig. 1. Two sets of data are given, differing in the stability exponent of the periodic orbit (which is easily adjusted by varying the middle strip width  $w_1$ ). The two values used were  $\lambda = \log 5$  (upper curve) and  $\lambda = \log 10$  (lower curve). In each case, the numerical data comes from an ensemble average over systems of size  $N = 1/h = 200$ . The errorbars shown in the figure

<sup>3</sup>For a billiard system, the analogous procedure would be to take a given short periodic orbit and then create an ensemble of systems by deforming the boundary in such a way that the original orbit is unaffected.

are statistical, and do not reflect finite-size effects. The theoretical curves are obtained from Eq. 45 and require only the single parameter  $\lambda$ . The agreement between theory and data is quite good; furthermore we see just how large the correlations are even for not very small exponents. Thus, for an orbit with a stretching factor of 10 per iteration ( $\lambda = \log 10$ ), the correlation does not go below 0.95 even for the maximally unrelated wavepackets ( $z = 1/2$ ).

In Fig. 2 we plot this minimum correlation  $C_{ab}(z = 1/2)$  on the vertical axis, versus the scarring enhancement factor  $g(\lambda)$  on the horizontal axis. Four data points are used, corresponding (from left to right) to stretching factors  $e^\lambda = 20, 10, 5, 2.5$ . Both the expected average enhancement  $g$  and the inter-wavepacket correlation  $C_{ab}(z = 1/2)$  are uniquely given theoretically as functions of the exponent  $\lambda$ . Again, the data agrees very well with the theoretical predictions. We see that a scarring enhancement factor of 2 (corresponding to stretching exponent  $\lambda \approx \log 5$ ) is associated with a *minimum* correlation of 0.99 between *the least correlated* wavepackets on that orbit. Strong scarring thus automatically eliminates the ambiguity in measuring the strength of Gaussian wavepacket scarring.

The question then becomes whether it is possible in any way to take advantage of our knowledge of the orbit and its invariant manifolds to produce a scarring test state that would do better than a single Gaussian wavepacket. Indeed, this is possible, and what is necessary is to use *coherent* quantum superpositions of test states [30,24,27] instead of the density matrix approach investigated in this section.

## IV. COHERENT WAVEPACKET SUMS: ENHANCED SCARRING

### A. Theory

As suggested already in [12], we can construct a “linearized eigenstate”  $|\psi\rangle$  as a normalized coherent sum of Gaussian wavepackets centered on a periodic orbit. For a fixed point orbit, we write

$$\Psi = \mathcal{N} \int dt e^{-t^2/T_0^2} |a_{\sigma e^{\lambda t}}\rangle \quad (51)$$

(see Eq. 22).  $T_0$  is a linearized dynamics time cutoff as defined in Eq. 24, and the normalization constant  $\mathcal{N}$  ensures  $\langle \Psi | \Psi \rangle = 1$ . Just as was done for the density matrix in the preceding section, Eq. 51 can be generalized in a straightforward way to higher-period orbits and to continuous time. However, to make the presentation more transparent the examples here and in the following section are restricted to the case of a fixed point, the generalizations being left to Section VI.

If the dynamics away from the periodic orbit were exactly linear, we could take the cutoff  $T_0$  to infinity and obtain a stationary state with quasi-energy  $\phi$  (phase  $e^{-i\phi}$ ,

see Eq. 4): hence the name “linearized eigenstate”. In reality, a finite cutoff is necessary because the ratio of the size of the linearizable region of phase space  $A$  to  $\hbar$  is finite. However, if this ratio is large (as it will always be in the semiclassical limit  $\hbar \rightarrow 0$ ), most of the state  $\Psi$  maps to itself under Eq. 4, producing a large autocorrelation function at short times. In the case of Gaussian wavepacket scarring, the extent to which the short-time return probability differs from unity (and thus the extent to which perfect localization fails to be achieved) is determined by the instability of the orbit (i.e. by the amount by which  $\lambda$  is different from zero). As measured using the improved test state  $\Psi$ , the absence of complete localization is given by the failure of the *linearized* dynamics at long times.

The test state  $\Psi$  lives not only at the periodic point, but also along the invariant manifolds. Its autocorrelation  $\langle \Psi | \Psi(t) \rangle$  decays only on the order of the *log-time*  $T_0 \sim \lambda^{-1} \log A/\hbar$ , as we show explicitly below in Eq. 55. This makes  $\Psi$  a much sharper measure of the scar character of an eigenstate, and for small  $\hbar$  we expect to see much stronger localization as measured by  $\Psi$  than by an individual wavepacket  $|a_\sigma\rangle$ . We will now proceed to show this explicitly. The construction of  $\Psi$  is extremely simple, requiring only one piece of information beyond what we already needed for the single wavepacket, namely the (approximate) size of the region in which the dynamics is linearizable. No knowledge of long-time dynamics, nonlinear recurrences, or any other periodic orbits is needed.

We also notice that in the strong scarring limit  $\lambda \rightarrow 0$ , we could just as well have used only the linearized time iterates of  $|a\rangle$  (rather than wavepackets of all widths) as in Eq. 51 to construct the hyperbolic test state:

$$\Psi_{\text{dyn}} \sim \sum_t e^{-t^2/T_0^2} |a_{\sigma e^{\lambda t}}\rangle = \sum_t e^{-t^2/T_0^2} e^{i\phi t} |a_{\text{lin}}(t)\rangle \quad (52)$$

(cf. Eq. 30). This form makes manifest the close connection between the construction of the scarring test state and the linearized classical dynamics (Eq. 2). It also makes almost trivial the generalization to higher period orbits and to continuous time (see Eq. 30 and also the fuller discussion in Section VI). The main disadvantage of the form  $\rho_{\text{dyn}}$  (as compared to  $\rho$ ) is that the former requires the arbitrary choice of initial width  $\sigma$ . However, as we have seen in the previous section, this choice of starting wavepacket has no effect on any measured quantities in the  $\lambda \rightarrow 0$  limit (where replacement of the integral by a sum is justified).

We begin as in Section II by evaluating the short-time autocorrelation function

$$A_{\text{lin}}^\Psi(t) \equiv \langle \Psi | U_{\text{lin}}(t) | \Psi \rangle. \quad (53)$$

A straightforward calculation using Eqs. 4, 6 gives:

$$A_{\text{lin}}^\Psi(t) = Q e^{-i\phi t} \int dy \frac{e^{-(t-\frac{y}{\lambda})^2/T_0^2}}{\sqrt{\cosh y}}. \quad (54)$$

The overall normalization constant  $Q$  can be fixed by requiring  $A_{\text{lin}}^\Psi(0) = \langle \Psi | \Psi \rangle = 1$ . The integration variable  $y$  is a time variable scaled by  $\lambda$  to make it dimensionless. In the limit  $T_0\lambda \gg 1$ , i.e.  $\log \frac{A}{\hbar} \gg 1$ , the exponential simplifies and we obtain

$$\begin{aligned} A_{\text{lin}}^\Psi(t) &= Q e^{-i\phi t} \int dy \frac{e^{-t^2/T_0^2}}{\sqrt{\cosh y}} \\ &= e^{-i\phi t} e^{-t^2/T_0^2}. \end{aligned} \quad (55)$$

Now we see explicitly that the decay rate of our test state  $\Psi$  is indeed given by the log-time scale  $T_0$ . Of course for the *linear* autocorrelation function to be a good measure of the *total* return amplitude  $A^\Psi(t)$ , even for times  $t$  less than  $T_0$ , the state  $\Psi$  must be well contained inside the linear region. This can be done by adjusting the constant  $c$  in Eq. 24: numerically we will see below that good quantitative agreement with Eq. 54 is obtained for  $c \approx 0.6$ . In any case, the precise value of this constant does not affect any of the important scaling arguments which will follow.

As in Section II, the inverse participation ratio has an enhancement factor associated with the short time recurrences:

$$\text{IPR}_\Psi \equiv \frac{\langle |\langle n | \Psi \rangle|^4 \rangle}{\langle |\langle n | \Psi \rangle|^2 \rangle^2} \quad (56)$$

$$= F \sum_t |A_{\text{lin}}^\Psi(t)|^2 \quad (57)$$

$$\approx F \sqrt{\pi} T_0, \quad (58)$$

where in the last line the limiting form Eq. 55 has been used, and  $T_0$  taken to be large. In the Gaussian wavepacket case, the IPR scaled with the orbit decay time  $\lambda^{-1}$ ; here it scales with the log-time  $\sim \lambda^{-1} |\log \hbar| \gg \lambda^{-1}$ . This makes the coherent test state a factor of  $T_0\lambda/\sqrt{\pi} \sim |\log \hbar|$  times better than any of the single Gaussian test states.

We can also look at the spectral envelope  $S_{\text{lin}}^\Psi$  which is the fourier transform of the short-time autocorrelation function (see Eq. 16):

$$S_{\text{lin}}^\Psi(E) = \sum_t A_{\text{lin}}^\Psi(t) e^{iEt} \quad (59)$$

$$\approx \sqrt{2\pi} T_0 e^{-(E-\phi)^2 T_0^2/2}, \quad (60)$$

where again in the last line the limiting ( $\hbar \rightarrow 0$ ) form Eq. 55 has been used. The energy envelope is centered at  $E = \phi$ , just like the smoothed single-wavepacket local density of states, but the the peak is both narrower and taller by a factor scaling as  $|\log \hbar|$ .

## B. Numerical Tests

We now check the results obtained in this section, using again the ensemble of kicked-baker systems introduced in

Section III C. The short periodic orbit will again be the fixed point of the middle baker's strip, with exponent  $\lambda$  set by the logarithm of the width of this strip. We begin by looking at the smoothed local densities of states  $S_{\text{lin}}^\Psi$  and  $S_{\text{lin}}^a$ , for the universal test state  $|\Psi\rangle$  and the simple Gaussian  $|a\rangle$ , respectively. The width  $\sigma$  of the starting Gaussian is set to  $\sqrt{w_1}$ , so that the aspect ratio of the Gaussian is equal to the aspect ratio of the rectangular middle strip in which the classical dynamics is linearizable. The wavepacket can then expand the same number of steps in either time direction before reaching the edge of the linear regime. The test state  $\Psi$  is constructed using a cutoff set by  $c = 0.6$  (see Eq. 24).

Ensemble averaging is performed over many kicked-baker systems of the same (reasonably large) exponent  $\lambda = |\log 0.18|$ , and of system size (Hilbert space dimension)  $N = 1/h = 800$ . Local densities of states for  $|a_\sigma\rangle$  and  $|\Psi\rangle$  are ensemble-averaged and smoothed, with the resulting envelopes plotted in Fig. 3. Theoretical curves obtained from Eqs. 16, 59 are also plotted for comparison. Excellent agreement is observed between the data and the predictions based on the linearized theory. Furthermore, we see that the spectral envelope for the hyperbolic test state  $\Psi$  is significantly narrower and taller than the corresponding envelope for the Gaussian wavepacket, again in accordance with prediction. We should note here that the hyperbolic test state is constructed here with the very modest log-time cutoff  $T_0 = 0.90$ . There are three reasons for the smallness of  $T_0$  in this example: 1) the stretching factor  $e^\lambda \approx 5.6$  is rather large, 2) the system size, and particularly the size of the linearizable region, are modest, 3) and finally the free parameter  $c$  has been set at a rather conservative (small) value. With regard to the last point, we should note in particular that increasing the cutoff parameter  $c$  (Eq. 24) will give rise to a sharper envelope, with larger inverse participation ratio, though at some cost to the accuracy of the formulas Eqs. 57, 59, etc. In effect, there is a tradeoff between keeping the test state well inside the linear region and thus being able to obtain with good accuracy its statistical properties (smaller  $c$ ) versus maximizing the localization properties of the hyperbolic test state by allowing it to some extent to leak out of the linear region (larger  $c$ ). All of this will become clearer as we go on to discuss IPR measures for the universal test states. Of course, none of these  $O(1)$  considerations affect the basic scaling predictions: namely the height, inverse width, and IPR of the spectral envelope for  $\Psi$  all scale inversely with  $\lambda$  for small  $\lambda$  and also logarithmically with  $1/h$  for small  $h$ . In particular, the hyperbolic (coherent  $\Psi$  test state) spectral envelope gets arbitrarily taller and narrower as  $h \rightarrow 0$  for a fixed classical system, while the corresponding spectral envelope for a single Gaussian packet test state remains unchanged.

We next probe the behavior of the mean  $\text{IPR}_\Psi$  as a function of  $N$  and  $c$  (with exponent  $\lambda$  again set to  $|\log 0.18|$ ). In Fig. 4, we plot the IPR versus cutoff time  $T_0$ , for five sets of data:  $N = 1/h = 50, 100, 200, 400$ , and

800 from bottom to top. For each value of  $N$ , 26 values are plotted: from left to right  $c = (1.1)^j$ ,  $j = -20 \dots +5$ . The five values at  $T_0 = 0$  represent simple Gaussian test states ( $c \rightarrow 0$ ). The upper dashed curve represents the theoretical prediction of Eq. 57, which should hold for large values of  $N$ . Good agreement with the data is obtained for  $N \geq 200$ , as finite-size effects become less relevant.<sup>4</sup> The six rightmost points on each data curve represent  $c \geq 1$ , and some deviation from the linear theory prediction is expected to start setting in there. We also note that at very large values of  $T_0$  (requiring correspondingly larger values of  $\log N$ ), the theoretical prediction converges to the linear asymptotic form of Eq. 58 (lower dashed line).

We note for purposes of comparison that the single-wavepacket scarring strength  $\text{IPR}_a$  is predicted to be 3.66 for this value of  $\lambda$  (see Eq. 20, noting that a quantum fluctuation factor  $F = 2$  is appropriate for complex eigenstates). This indeed is close to the value attained by the single wavepackets ( $T_0 = 0$ ), at least for  $N \geq 200$ .<sup>5</sup> We see that IPR values significantly larger than this can be attained using the hyperbolic test states, especially for larger values of  $N$ . The data is consistent with the prediction that the IPR (at fixed value of  $c \sim 1$ ) scales logarithmically with  $N$  for large system size  $N$ .

Finally, to close this section we present in Fig. 5 the Husimi phase-space plot for the hyperbolic test state  $\Psi$ . In this figure,  $T_0$  has been taken to be very large compared to  $\lambda^{-1}$ , i.e. the linearizable regime is much larger than a unit Planck cell, and also much larger than the phase-space area shown in the figure. We note that the phase-space Husimi picture is universal, and in particular independent of the exponent  $\lambda$ , since a change in the value of  $\lambda$  in Eq. 51 can of course always be absorbed into a redefinition of  $T_0$  and the overall normalization  $\mathcal{N}$ . In other words, in the  $\log \frac{A}{h} \rightarrow \infty$  limit, the state  $\Psi$  depends only on the linear region size parameter  $A/h$ , and when we further look well inside the area  $A$ , its structure is completely free of any parameters. The phase space area shown in the figure is  $12\sqrt{h} \times 12\sqrt{h}$ , i.e. it contains  $144/2\pi$  Planck-sized cells. We see from the Figure that  $\Psi$  lives at the periodic point in the center of the plot (the size of the bright region at the periodic point being set by  $h$ ), and symmetrically along the linearized stable and unstable manifolds. This picture will be important to us for comparison purposes when we study off-resonance universal test states in the following section. The analytic expression used to obtain the density plot in Fig. 5

<sup>4</sup>Notice that because the width of the central strip here is quite small (0.18),  $N = 200$  corresponds to a size of only  $0.18 \times 200 = 36$  for the linearizable region (in units of  $h$ ).

<sup>5</sup>The deficit in the measured single Gaussian IPR values ( $T_0 = 0$ ) for finite  $N$ , i.e. the extent to which these fall below the limiting value of 3.66, is in close correspondence with similar deficits in the hyperbolic state IPR's ( $T_0 > 0$ ).

will also be given there (Eq. 64).

## V. OFF-RESONANCE AND OFF-ORBIT SCARRING

Going back to the construction of the hyperbolic test state  $\Psi$  in Eq. 51, we notice that there the Gaussian wavepackets are all added *in phase*, giving rise to a preferred energy  $\phi$  which is the same as that for any single wavepacket considered individually. We may, however, equally well consider the more general form

$$\Psi = \mathcal{N} \int dt e^{-t^2/T_0^2} e^{i\theta t} |a_{\sigma e^{\lambda t}}\rangle, \quad (61)$$

where  $\theta$  is an arbitrary phase accumulated per time step. This extra phase should give rise to a state that prefers to live at an energy different from the one that exactly quantizes the periodic orbit (i.e.  $E = \phi$ ). In turn, this energy shift may be expected to give rise to phase space structures that lie away from the invariant manifolds of the periodic orbit, i.e. above and below the separatrix constructed from these manifolds [29]. These intuitive expectations turn out to be justified, as we now shall see.

We begin once again by computing the short-time (linearized) autocorrelation function. The generalization of Eqs. 54, 55 works out to be:

$$A_{\text{lin}}^{\Psi}(t) = Q e^{-i\phi t} \int dy \frac{e^{-(t-\frac{y}{\lambda})^2/T_0^2 - i\theta(t-\frac{y}{\lambda})}}{\sqrt{\cosh y}} \quad (62)$$

$$\approx e^{-i(\phi+\theta)t} e^{-t^2/T_0^2}. \quad (63)$$

In the last line, the limits  $\lambda \rightarrow 0$  and  $T_0\lambda \sim \log \frac{A}{\hbar} \rightarrow \infty$  have been taken, in complete analogy with Eq. 55.

From these expressions, we proceed to obtain spectral envelopes and IPR values, exactly as we did previously for the  $\theta = 0$  special case. It is interesting to note here that in the asymptotic limit of Eq. 63, the spectral envelope will be exactly the same as that obtained previously (Eq. 60), but shifted so as to be centered at energy  $E = \phi + \theta$ . Because the shape of the envelope is unaffected by the value of  $\theta$  in this limit, the IPR is still asymptotically given by our previous formula, Eq. 58. It is important to note, however, that for realistic values of  $\log \frac{A}{\hbar}$ , this asymptotic regime may not be attained, and the more general formulas Eqs. 57, 59, 62 should be used instead.

In Fig. 6, we plot (numerically obtained) smoothed spectral envelopes for the hyperbolic states  $\Psi$ , for the same ensemble of systems as was used in producing Fig. 3. The envelopes correspond to  $\theta = 0$  (the tallest envelope, already seen previously in Fig. 3), through  $\theta = -2\pi$ , moving to the left in steps of  $2\pi/20$ . Even though the asymptotic form of Eq. 63 predicts all the envelopes should have the same shape, being merely shifted to the left by angle  $\theta$ , in reality we see this is not quite

the case for finite values of  $\log(A/\hbar)$ . Because of the finite linearizable volume of phase space, the off-resonance hyperbolic states have significantly less well-defined envelopes compared to the  $\theta = 0$  state. That is because the asymptotic form assumes most of the autocorrelation function comes from long-time overlaps of wavepackets with very different widths. At finite system sizes, a very important correction is the partial self-cancellation in  $\Psi$  coming from wavepackets of comparable widths being added together with very different phases. This correction is, of course, taken into account in the more general form of Eq. 62, which does in fact predict less sharp envelopes (and consequently lower IPR's) for the off-resonance states. The important point to notice here, however, is the presence of a very significant localization effect even for  $|\theta| > \lambda$ , i.e. at energies well outside the resonance of the original Gaussian wavepacket. States at such energies are not strongly scarred according to the original (Gaussian wavepacket) definition, nor are they particularly enhanced along the stable and unstable manifolds of the orbit, as measured by the on-resonance hyperbolic test state. However, such states do have enhanced intensity relative to the off-resonance hyperbolic states  $\Psi(\theta \neq 0)$ , which live in hyperbolic regions on either side of the separatrix (see Fig. 10 later in this section). Although the enhancement factors for such states are quite modest for the parameters chosen ( $\sim 2$  over RMT), they will of course grow with  $\lambda^{-1}$  and with  $\log A/\hbar$ , as we discussed earlier. In particular, in the high energy limit ( $\hbar \rightarrow \infty$ ) of a given classical system, scarring by the off-resonance states is expected to be equally strong compared to the on-resonance ( $\theta = 0$ ) form of scarring.

To demonstrate the preceding assertion, we plot in Fig. 7 the (theoretically computed) IPR as function of  $T_0$ , for several values of the off-resonance angle  $\theta$ . To facilitate comparison with Fig. 4, we again choose stretching exponent  $\lambda = |\log 0.18|$ . The six curves represent (from top to bottom at  $T_0 = 1$ ) values of  $\theta$  from 0 to  $\pi$ , in steps of  $\pi/5$ . The top curve has thus already appeared previously in Fig. 4. The lowest curve will later be compared with data in Fig. 8. The asymptotic form of Eq. 58, to which all these curves converge at large  $T_0$  (large  $|\log \hbar|$ ), is shown in the figure as a dashed line.

An interesting point to notice here is that for sufficiently large  $\theta$ , the IPR can drop at moderate  $T_0$  from its single-wavepacket value (at  $T_0 = 0$ ), before eventually recovering at larger  $T_0$  (this is a result of the self-cancellation effect alluded to earlier). However, for (exponentially) large systems, scarring is equally strong for the different values of the off-resonance parameter  $\theta$ . Intuitively, for a large system (or small  $\hbar$ ), the size of the linearizable region in which the test state  $\Psi$  is constructed is very large compared to the size ( $\sim \hbar$ ) of a single wavepacket. Thus, a given wavepacket used into the construction of  $\Psi$  in Eq. 61 has very little overlap with most of the other wavepackets in the sum. For this reason, the cancellation effect arising from similar

wavepackets being added together with different phases (for non-zero  $\theta$ ) becomes insignificant in the semiclassical limit.

To make contact once again with the data, we choose  $\theta = \pi$ , and in Fig. 8 do for this case what we did for  $\theta = 0$  earlier in Fig. 4. Again, data for  $N = 50, 100, 200, 400$ , and  $800$  is plotted, and the same range of  $c$ -values is used. Only for  $N \geq 200$  do we see the recovery towards larger IPR values that we expect from the theoretical curve (dashed). Recall that 3.66 is the single-wavepacket IPR value.

In Fig. 9, the system size  $N = 200$  is fixed, with cutoff parameter  $c = 0.6$ , and the IPR is plotted versus the off-resonance angle  $\theta$ , ranging here from  $0$  to  $2\pi$ . Agreement between theory and data is in this case (surprisingly) good. We see for this value of  $N$  that by  $\theta = 2\pi$ , the IPR values are already approaching the RMT value of  $2$ , indicating almost no localization.

Finally, we return to the Husimi representation of  $\Psi$ , which we began to discuss already in the previous section. Husimi representations of the off center scarring were discussed in [29], where the inverted oscillator eigenstates were probed with Husimi states. Here, we have shown how to generate test states which are sensitive to off-center scars developing in chaotic systems. For reference, the expression describing the Husimi intensities is:

$$H_{q_0, p_0}^\Psi = |\langle g_{q_0, p_0} | \psi \rangle|^2 = e^{-q_0^2/\hbar} \left| \int dy \frac{e^{-y^2/\lambda^2 T^2} e^{iy\theta/\lambda} e^{\frac{(q_0 - ip_0)^2 e^y}{4\hbar \cosh y}}}{\sqrt{\cosh y}} \right|^2. \quad (64)$$

Here  $g_{q_0, p_0}$  is a phase-space Gaussian centered at phase-space point  $(q_0, p_0)$  of width  $\sqrt{\hbar}$  in both position and momentum:

$$g_{q_0, p_0}(q) = (\pi\hbar)^{-1/4} e^{-(q-q_0)^2/2\hbar + ip_0(q-q_0)/\hbar}. \quad (65)$$

Recall that we are working in a coordinate system where the fixed point is located at the origin  $(q, p) = (0, 0)$ , and the linearized invariant manifolds are horizontal and vertical (Eq. 2). As the linearizable region becomes large compared to the phase space region of interest ( $T_0 \rightarrow \infty$ ), the Husimi density of Eq. 64 depends on only three dimensionless numbers: an off-resonance parameter  $\theta/\lambda$  and the phase space coordinates  $q_0/\sqrt{\hbar}$ ,  $p_0/\sqrt{\hbar}$ .

Previously, in Fig. 5, we have seen the Husimi density of  $\Psi$  for  $\theta/\lambda = 0$  plotted in the square phase space area  $-6 \leq q_0/\sqrt{\hbar}, p_0/\sqrt{\hbar} \leq +6$ . In Fig. 10 we present the analogous picture for (a)  $\theta/\lambda = 0.8$ , and (b)  $\theta/\lambda = 2.5$ . As the energy goes further off resonance, the state  $\Psi$  moves away from the periodic orbit and its invariant manifolds, and shifts into two of the quadrants separated by the manifolds ( $qp > 0$  or  $qp < 0$ , depending on the sign of  $\theta$ ). For large  $|\theta|/\lambda$ , narrow hyperbolic regions in phase space are accessed, lying further and further from the periodic orbit itself. For  $\theta/\lambda \sim \pm 1$ ,  $\Psi$  lives

near the hyperbolas  $qp \sim \pm\hbar$  surrounding the periodic point. This regime corresponds to a spectral envelope for  $\Psi$  which is centered at energy  $\lambda$  away from the EBK energy, i.e. at the edge of the single-Gaussian spectral envelope. Eigenstates having strong overlaps with  $\Psi$  are now barely scarred at the periodic point itself. If we go further into the regime  $|\theta|/\lambda \gg 1$ , the spectral envelope of  $\Psi$  is now centered at an energy which is outside the envelope of the single wavepacket. Then, states overlapping such a test state  $\Psi$  will have stronger than expected intensity on hyperbolic regions surrounding the periodic orbit, but will not be scarred at all (and may even be antiscarred) on the orbit itself.

The connection discussed above between an energy shift away from the EBK value and hyperbolic phase-space structures may be understood very simply by considering the evolution of off-center Gaussians  $g_{q_0, p_0}$  of Eq. 65. Such a Gaussian is not an optimal test state for measuring scarring, because the autocorrelation function decays quite rapidly, especially for  $q_0^2 + p_0^2 \gg \hbar$  (to be contrasted with  $\Psi$ , which lives along the *entire* hyperbolic region, and thus has much larger self-overlaps at short times). However, the phase information in the autocorrelation function for  $g_{q_0, p_0}$  is quite relevant:

$$A_{\text{lin}}(t) = e^{-i\phi t} e^{-\frac{q_0^2 + p_0^2}{\hbar} \frac{\sinh^2 \lambda t/2}{\cosh \lambda t}} e^{-\frac{iq_0 p_0}{\hbar} \tanh \lambda t} \quad (66)$$

(compare with Eq. 6). Upon Fourier transforming this to obtain a spectrum, we obtain an expression for the optimal energy as a function of phase-space location:

$$E - \phi \approx \lambda \frac{qp}{\hbar}. \quad (67)$$

Thus the off-resonance parameter  $\theta$  of our test state  $\Psi$  is then expected to be associated with phase-space hyperbolas:

$$\frac{\theta}{\lambda} \approx \frac{qp}{\hbar}. \quad (68)$$

## VI. EXTENSION TO HIGHER-PERIOD ORBITS AND CONTINUOUS TIME

### A. Longer orbits of maps

The analysis of the previous two sections has focused on fixed-point periodic orbits, but it generalizes in a straightforward way to longer orbits and to continuous time. We shall see below that the benefits of using universal scar measures instead of simple Gaussians become even greater when longer orbits are considered.

Consider again a periodic orbit (of a map) of period  $T_P$ , with periodic points  $x_p$  ( $p = 0 \dots T_P - 1$ ), as in Eq. 26. Let  $-\phi$  be the phase accumulated over one full iteration of the orbit, and  $\lambda$  the corresponding stability exponent. The short-time autocorrelation function for a

Gaussian  $|a\rangle$  centered at any of the periodic points is a generalization of Eq. 6:

$$A_{\text{lin}}(t) = \frac{e^{-i\phi t/T_P}}{\sqrt{\cosh \lambda t/T_P}} \delta_{(t \bmod T_P), 0}. \quad (69)$$

The IPR as function of  $\lambda$  is then the same as for a period-one orbit (because it is given simply by the sum of the short-time return probabilities, Eq. 19), while the short-time spectral envelope  $S_{\text{lin}}$  has  $T_P$  peaks in the quasienergy domain  $[0, 2\pi]$ , of height scaling as  $\lambda^{-1}$ , and width scaling as  $\lambda/T_P$ . The peak energies are of course those that ‘quantize’ the orbit:  $T_P E = \phi \bmod 2\pi$ , or

$$E_k = \frac{\phi + 2\pi k}{T_P}, \quad k = 0 \dots T_P - 1. \quad (70)$$

We notice that both the maximum scarring strength and the IPR can be large only for small  $\lambda$ , which becomes difficult to achieve for the longer orbits  $T_P > 1$  (normally  $\lambda$  grows linearly with  $T_P$ ).

We now proceed to construct the universal test state  $\Psi$  for such an orbit, having made a choice of quantization energy  $E_k$ :

$$\begin{aligned} \Psi = \mathcal{N} \sum_p \int dt e^{-t^2/T_P^2 T_0^2} \\ \times e^{i(E_k + \theta/T_P)p + i\theta t/T_P - i\phi_p} |a_{x_p, \sigma f_p e^{\lambda t/T_P}}\rangle. \end{aligned} \quad (71)$$

Here  $f_p$  is a stretching factor, and  $\phi_p$  is a phase, both defined by

$$U_{\text{lin}}^p |a_{x_0, \sigma}\rangle = e^{-i\phi_p} |a_{x_p, \sigma f_p e^{\lambda p/T_P}}\rangle. \quad (72)$$

$f_p$  and  $\phi_p$  take into account the fact that stretching and phase accumulation along the orbit may both be non-uniform; of course,  $f_{T_P} = 1$  and  $\phi_{T_P} = \phi$ . The factors  $f_p$  are of order unity and thus not very important in the semiclassical limit  $\log A/\hbar \rightarrow \infty$  when the linearizable region is very large; on the other hand, the phases  $\phi_p$  are crucial for getting constructive interference. The parameter  $T_0$  is defined as before (Eq. 24), using the area of the linearizable region around periodic point  $x_0$ , and  $\theta/\lambda$  is an off-resonance parameter, as discussed previously.

The short-time autocorrelation function of the state  $\Psi$  then has the same form as what we found previously for the special case  $T_P = 1$  (Eqs. 54, 55, 62, 63), replacing

$$T_0 \rightarrow T_0 T_P, \quad \lambda \rightarrow \lambda/T_P, \quad \theta \rightarrow \theta/T_P, \quad \phi \rightarrow E_k \quad (73)$$

throughout. Note that  $\lambda$  and  $\theta$  are defined as stretching exponent and phase *per orbit period* rather than per time step, and likewise  $T_0$  is the log-time measured in units of the orbit period. Eqs. 59, 60 describing the shape of the linear spectral envelope, and Eqs. 57, 58 for the IPR of the universal test state  $\Psi$  undergo the same simple modifications and are then applicable to the case of  $T_P > 1$ .

Let us compare these results with ordinary (single Gaussian) scarring for  $T_P > 1$  as well with the scarring of a fixed point, which we focused on in the previous two sections.

For general  $T_P \geq 1$ , the autocorrelation function of a Gaussian wavepacket  $|a_\sigma\rangle$  has  $O(\lambda^{-1})$  strong recurrences spaced  $T_P$  steps apart, and thus stretching over a total time scale of order  $T_P \lambda^{-1}$ . In the quasienergy domain, this leads to a set of  $T_P$  evenly spaced spectral envelopes, each with width, height, and IPR scaling (for small  $\lambda$ ) as:

$$\begin{aligned} w_a &\sim \lambda/T_P \\ h_a &\sim \lambda^{-1} \\ \text{IPR}_a &\sim \lambda^{-1} \end{aligned} \quad (T_P \text{ envelopes, centered at all } E_k). \quad (74)$$

Although the width scales with the exponent *per time step*, due to the presence of  $T_P$  of these envelopes, the maximum expected scarring strength and the IPR both scale only with the total exponent *per iteration of the entire orbit*, and thus are expected to deviate less and less from perfect ergodicity as longer orbits are considered.

Let us repeat the same analysis for the state  $\Psi$ , which takes properly into account all of the linearized dynamics around the periodic orbit. The short-time autocorrelation function does not decay until a time of order  $T_0 T_P \sim T_P \lambda^{-1} \log A/\hbar$ . This produces a *single* peak centered at quasienergy  $E_k$  (or shifted by an off-resonance phase  $\theta/T_P$ ). The width, height, and IPR scale as

$$\begin{aligned} w_a &\sim \lambda/(T_P \log A/\hbar) \\ \text{IPR} &\sim h_a \sim (T_P \log A/\hbar)/\lambda \\ (1 \text{ envelope, centered at some } E_k + \frac{\theta}{T_P}). \end{aligned} \quad (75)$$

Apart from the logarithmic enhancement which leads to more and more deviation from RMT in the  $\hbar \rightarrow 0$  limit, we also notice that only one peak is present (a choice of quantization energy  $E_k$  having been made), and all quantities now depend only on the ratio  $\lambda/T_P$ , the stability exponent *per time step*. This measure of scarring therefore allows us to see strong effects even for longer periodic orbits, as long as the stretching per time step remains moderate.

If the total exponent  $\lambda$  (and not just  $\lambda/T_P$ ) is small, we can equivalently use the linearized dynamics to generate our universal test state (compare Eqs. 30, 52). Eq. 52 generalizes easily to

$$\Psi_{\text{dyn}} \sim \sum_t e^{-t^2/T_P T_0^2} e^{i(E_k + \theta/T_P)t} |a_{\text{lin}}(t)\rangle, \quad (76)$$

where  $|a\rangle$  is a Gaussian wavepacket of width  $\sigma$  centered at any point along the periodic orbit. Eq. 71 can be thought of as an averaging of Eq. 76 over the initial width  $\sigma$  from some  $\sigma_0$  to  $\sigma_0 e^\lambda$ . For small  $\lambda$ , the averaging procedure is unnecessary, all the states being essentially identical, and the simple expression of Eq. 76 well describes the universal test state for any choice of  $\sigma$ .

## B. Hamiltonian systems

The entire analysis can be applied also to Hamiltonian systems in an essentially unchanged form. Let  $T_P$  again be the period of the orbit (now measured in real time units rather than in time steps), and let  $\lambda$  and  $\phi$  still be the exponent and phase per one iteration of the orbit. Then an optimal Gaussian centered anywhere on the orbit and aligned along the stable and unstable manifolds (with width  $\sigma$  along the unstable manifold) has a linear autocorrelation function given by a sum over iterations of the orbit:

$$A_{\text{lin}}(t) = \sum_n w(t - nT_P) \frac{e^{-i\phi n}}{\sqrt{\cosh \lambda n}}. \quad (77)$$

The very-short-time window function  $w(t)$  describes the self-overlap of the wavepacket as it intersects itself once every period; it is associated with the nonzero width  $\sigma_x$  of the wavepacket in the direction of the orbit, and has a scale  $\Delta t \sim \sigma_x/v \sim \sigma_x/\sqrt{E}$ . (In the last equality, the particle mass has been assumed to be unity, as it will be throughout.) Fourier transforming, we obtain a very wide envelope (of width  $\Delta E \sim \hbar\sqrt{E}/\sigma_x$ ) associated with the energy uncertainty of the wavepacket itself. Multiplying this are the scarring envelopes, centered at the quantizing energies, of width<sup>6</sup>

$$w_a \sim \hbar\lambda/T_P, \quad (78)$$

and separated by

$$s_a \sim \hbar/T_P. \quad (79)$$

The normalized peak height, and the IPR are therefore given by

$$\text{IPR} \sim h_a \sim \lambda^{-1}. \quad (80)$$

Again we see that ordinary measures of scarring are typically unable to resolve scarring arising from longer orbits, because the exponent  $\lambda$  for such orbits is generally not small.

The universal state  $\Psi$  is constructed by analogy with Eq. 71 as

$$\Psi = \mathcal{N} \int_0^{T_P} d\tau \int dt e^{-t^2/T_P^2 T_0^2} \times e^{i(E_k + \hbar\theta/T_P)\tau/\hbar + i\theta t/T_P - i\phi\tau} |a_{x_\tau, \sigma_x, \sigma_{f_\tau}} e^{\lambda t/T_P}\rangle. \quad (81)$$

Here  $\tau$  is a time parameter parametrizing the orbit  $x_\tau$ ,  $f_\tau$  and  $\phi_\tau$  are as before a stretching factor and phase

associated with short time evolution from  $x_0$  to  $x_\tau$ ,  $E_k$  is a quantization energy, and  $\theta/\lambda$  is again an optional off-resonance energy shift parameter. For small  $\lambda$ , this can be written as

$$\Psi_{\text{dyn}} \sim \sum_t e^{-t^2/T_P^2 T_0^2} e^{i(E_k + \hbar\theta/T_P)t/\hbar} |a_{\text{lin}}(t)\rangle. \quad (82)$$

The short-time autocorrelation function again has a decay time scale  $T_P T_0 \sim T_P \lambda^{-1} \log A/\hbar$  (with no window  $w(t)$  present), leading to a *single* spectral envelope centered at energy  $E_k$  ( $E_k + \hbar\theta/T_P$  for off-resonance states), and of width and height given by

$$\begin{aligned} w_\Psi &\sim \hbar\lambda/(T_P \log A/\hbar) \\ h_\Psi &\sim (T_P \log A/\hbar)/\hbar\lambda. \end{aligned} \quad (83)$$

The IPR is somewhat difficult to talk about in this case because IPR's (like any other measure of quantum ergodicity) can only be measured relative to some already known energy window which takes into account various conserved quantities. In this case, the only plausible window is the spectral envelope of the original Gaussian wavepacket of width  $\sigma_x$  in the direction of the periodic orbit (see discussion following Eq. 77). Then the IPR is given by

$$\text{IPR}_\Psi \sim \frac{\sqrt{E} T_P}{\lambda \sigma_x} \log \frac{A}{\hbar}. \quad (84)$$

Notice that the combination  $\lambda/\sqrt{E} T_P$  is just the exponent per unit length of the orbit. Of course, our result depends on the width  $\sigma_x$  of each Gaussian along the orbit. The enhancement of the IPR for  $\Psi$  over the corresponding IPR for the single Gaussian (Eq. 80) can also be thought of as being given by the usual logarithmic factor times the ratio  $\sqrt{E} T_P/\sigma_x$  of the length of the orbit compared to the wavepacket size.

In any case, we again see that long orbits can be easily resolved using this improved scarring measure. A sufficient condition to get significant enhancement is for the exponential stretching to be small on the time scale of the very-short-time window  $w(t)$ , i.e. during the time it takes for the wavepacket to traverse its width while moving along the orbit. This criterion is of course independent of the orbit length. Even if the criterion above is not satisfied at low energies, one nevertheless gets strong scarring in the semiclassical limit. For a two-dimensional billiard system, the increase in scarring strength (as measured by peak height of the spectrum or by the IPR) scales with energy as

$$h_\Psi \sim \sqrt{E} \log E \quad (85)$$

$$\text{IPR}_\Psi \sim E^{1/4} \log E. \quad (86)$$

(The power-law IPR scaling arises from the wavepacket width  $\sigma_x$  scaling with energy as  $\sigma_x \sim E^{-1/4}$ . This is a natural scaling which keeps the  $x$ -uncertainty and the

<sup>6</sup> Notice that  $E$  is now a real energy, rather than the Floquet phase it was for a map, and  $T_P$  has units of time instead of step number, hence the factor of  $\hbar$  in the equations following.

uncertainty in the  $x$ -momentum  $p_x$  in a fixed ratio relative to the total size of the accessible phase space. Without this scaling the increase in IPR with energy would be only logarithmic.)

### C. Numerical tests

We conclude this section with a numerical example of the localization enhancement obtainable for longer orbits using the universal test-state approach. For this purpose, we choose a modified version of the kicked-baker system introduced in Section III C. Instead of having the kicks act on the left and right strips of the three-strip system, we have one act now only on the middle strip, leaving the left and right strips to undergo ordinary baker-like dynamics, i.e. horizontal expansion and vertical compression. Any periodic orbits contained entirely in these two side strips thus have locally orthogonal stable and unstable manifolds (of the form Eq. 2), with a stretching exponent and action given simply in terms of the widths  $w_0$  and  $w_2$  of the left and right strips. In particular, consider the period-2 orbit that jumps from the left strip to the right strip and back. Its periodic point in the left strip is given by  $q = w_0(1 - w_2)/(1 - w_0w_2)$ ,  $p = (1 - w_2)/(1 - w_0w_2)$ . The other periodic point is obtained by interchanging the  $q$  and  $p$  coordinates. The stretching exponent for one full iteration of this orbit is  $\lambda = |\log w_0w_1|$ , and the corresponding phase is given by  $\phi = w_0(1 - w_2)^2/(1 - w_0w_2)\hbar$ . Thus, a desired value for the exponent and phase can be fixed by selecting the three baker strip widths, and the kick strength acting on the middle strip is then used to provide ensemble averaging over the details of the long orbits (nonlinear recurrences).

We select for our example widths  $w_0 = 0.40$ ,  $w_2 = 0.42$ , as before, leading to an exponent  $\lambda = |\log 0.168|$  for our chosen orbit, and work with the matrix size  $N = 800$ . In Fig. 11, the smoothed local density of states for a Gaussian wavepacket, obtained by averaging over several realizations, is represented by the double-peaked solid curve. The theoretical prediction, given by the linearized dynamics of Eq. 69, is shown by the dashed curve. The narrow, single-peaked solid curve centered at one of the two possible quantization energies is the similarly smoothed local density of states for the universal state  $\Psi$ , constructed once again with  $c = 0.6$  and  $\theta = 0$ , as in Fig. 3. Again, the corresponding dashed curve is the theoretical prediction based on the linearized dynamics and agrees well with the data. Notice that in this case the difference between Gaussian and universal scarmeters is more dramatic than in Fig. 3, the reason being that scarring as measured by  $\Psi$  depends only on the stretching rate along the unstable manifold per unit time, not per iteration of the entire orbit. While scarring strength as measured by a single wavepacket drops off with orbit length, scarring strength as measured by  $\Psi$  is length-independent as

long the orbit period remains small compared to the log-time. Orbits of arbitrary length can therefore be strongly scarred using this measure, provided a correspondingly small value of  $\hbar$  is chosen.

## VII. SUMMARY AND CONCLUDING REMARKS

In this paper we began by reviewing the theory and existing measures of scarring. We were then able to establish considerably refined and arguably universal scarring measures. The refinement means in practice that much larger deviations from RMT behavior are predicted using the refined test states. The test states are not special from the standpoint of random wavefunctions, but they pick up structures which exist in eigenstates of dynamical systems.

The two major issues of generalization of scar measures which we faced are 1) coherence (or lack of it) in superpositions of localized wavepacket states, and 2) summing over all the points of periodic orbits whose period is greater than one iteration of a map. The smooth Hamiltonian version of this is to coherently add up packets all along the orbit, making phase space tubes which are related to the tubes of Agam and Fishman [22]; see also [12].

The universality mentioned above stems ultimately from the use of the linearizable domain near periodic points in the construction of scar measures. The scar test states are the optimal ones which can be constructed with the linearized dynamics. In turn, we argued that the linearizable portion of the dynamics was a reasonable stopping point for the definition of scar strength. Going beyond the linearizable dynamics is certainly possible and semiclassically viable, but a problem arises in that one begins to approach the construction of individual eigenstates, at least in favorable cases [18], which is a somewhat disturbing limit. The reason this is disturbing is that such “test” states for scarring pick up (in the ideal limit) only one state, which brands the whole eigenstate as a scar. Moreover, pieces of classical manifolds far from any given periodic orbit will have been incorporated in the longer time dynamics of such a test state. Indeed it is not at all clear that any one periodic orbit should dominate the others in such a state. These new periodic orbits would begin to play a role in the long time dynamics (on the order of the Heisenberg time), so we would not even be speaking of a scar of a given periodic orbit. Given all these factors it seems reasonable to stop at the linearizable zone surrounding given periodic orbits.

Various numerical tests made possible by ensemble averaged baker map results supported the measures established here. The enhancements in IPR made possible by our optimized coherent measures can be modest (factors of 1.5 or 2) for reasonable  $\hbar$  and short orbits, but much more dramatic for longer period orbits, as compared to a single Gaussian wavepacket measure.

Finally, we have given a theoretical basis for the “off center” scars living on the hyperbolic manifolds near (but not on) a given periodic orbit, and provided them with test states sensitive to their presence.

### VIII. ACKNOWLEDGEMENTS

This research was supported by the National Science Foundation under Grants 66-701-7557-2-30 and CHE9610501.

---

[1] O. Bohigas, M.-J. Giannoni, and C. Schmit, *J. Physique Lett.* **45**, L-1015 (1984).  
[2] E. J. Heller, *Phys. Rev. Lett.* **53**, 1515-18 (1984).  
[3] S. W. McDonald, Ph.D. thesis, Lawrence Berkeley Laboratory, LBL14837 (1983).  
[4] S. W. McDonald and A. N. Kaufman, *Phys. Rev. Lett.* **42**, 1189 (1979).  
[5] M. V. Berry, *Ann. NY Acad. Sci.* **357**, 183 (1983).  
[6] E. B. Bogomolny, *Physica D* **31**, 169 (1988).  
[7] M. V. Berry, Les Houches Lecture Notes, Summer School on Chaos and Quantum Physics, M.-J. Giannoni, A. Voros, and J. Zinn-Justin, eds., Elsevier Science Publishers B.V. (1991); M. V. Berry, *Proc. Roy. Soc. A* **243**, 219 (1989).  
[8] A. D. Peters, C. Jaffe, and J. Delos, *Phys. Rev. A* **56**, 311 (1997).  
[9] T. M. Fromhold, P. B. Wilkinson, F. W. Sheard, L. Eaves, J. Miao, and G. Edwards, *Phys. Rev. Lett.* **75**, 1142 (1995); P. B. Wilkinson, T. M. Fromhold, L. Eaves, F. W. Sheard, N. Miura, and T. Takamasu, *Nature*, **380**, 608 (1996).  
[10] L. Kaplan, “Scar and antiscar quantum effects in open chaotic systems,” preprint.  
[11] P. O’Connor, J. N. Gehlen and E. J. Heller, *Phys. Rev. Lett.* **58**, 1296 (1987).  
[12] L. Kaplan and E. J. Heller, *Ann. Phys. (N. Y.)* **264**, 171 (1998).  
[13] L. Kaplan, *Phys. Rev. Lett.* **80**, 2582 (1998).  
[14] L. Kaplan, “Recent developments in the theory of scarring,” to appear in *Nonlinearity*.  
[15] A. I. Schnirelman, *Usp. Mat. Nauk.* **29**, 181 (1974).  
[16] S. Zelditch, *Duke Math. J.* **55**, 919 (1987).  
[17] Y. Colin de Verdiere, *Commun. Math. Phys.* **102**, 497 (1985).  
[18] S. Tomsovic and E. J. Heller, *Phys. Rev. Lett.* **70**, 1405 (1993).  
[19] L. Kaplan, *Phys. Rev. E* **58**, 2983 (1998).  
[20] T. M. Antonsen, Jr., E. Ott, Q. Chen, and R. N. Oerter, *Phys. Rev. E* **51**, 111 (1995).  
[21] M. A. Sepulveda, S. Tomsovic, and E. J. Heller, *Phys. Rev. Lett.* **69**, 402 (1992).  
[22] O. Agam and S. Fishman, *Phys. Rev. Lett.* **73**, 806 (1994); O. Agam and S. Fishman, *J. Phys. A* **26**, 2113

(1993); O. Agam and N. Brenner, *J. Phys. A* **28**, 1345 (1995); S. Fishman, B. Georgeot, and R. E. Prange, *J. Phys. A* **29**, 919 (1996).  
[23] B. Li and B. Hu *J. Phys. A* **31**, 483 (1998).  
[24] G. G. de Polavieja, F. Borondo, and R. M. Benito, *Phys. Rev. Lett.* **73**, 1613 (1994).  
[25] D. Klakow and U. Smilansky, *J. Phys. A* **29**, 3213 (1996).  
[26] A. M. Ozorio de Almeida, *Phys. Rep.* **295**, 265 (1998).  
[27] S. Tomsovic, *Phys. Rev. Lett.* **77**, 4158 (1996).  
[28] F. J. Arranz, F. Borondo, and R. M. Benito, *Phys. Rev. Lett.* **80**, 944 (1998).  
[29] S. Nonnenmacher and A. Voros, *J. Phys. A* **30**, 295 (1997).  
[30] F. P. Simonotti, E. Vergini, and M. Saraceno, *Phys. Rev. E* **56**, 3859 (1997).  
[31] N. L. Balazs and A. Voros, *Europhys. Lett.* **4**, 1089 (1987); N. L. Balazs and A. Voros, *Ann. Phys. (N. Y.)* **190**, 1 (1989); M. Saraceno, *Ann. Phys. (N. Y.)* **199**, 37 (1990); M. Saraceno and A. Voros, *Physica D* **79**, 206 (1994).  
[32] L. Kaplan and E. J. Heller, *Physica D* **121**, 1 (1998).  
[33] G. Casati, B. V. Chirikov, F. M. Izrailev, and J. Ford, in *Stochastic Behavior in Classical and Quantum Hamiltonian Systems*, ed. by G. Casati and J. Ford, Springer, New York (1979); M. V. Berry, N. L. Balazs, M. Tabor, and A. Voros, *Ann. Phys. (N. Y.)* **122**, 122 (1979).

FIG. 1. The correlation  $C_{ab}$  (Eq. 37) between local densities of states for two wavepackets  $|a\rangle$  and  $|b\rangle$ , lying on the same periodic orbit of instability exponent  $\lambda$ , is plotted as a function of width parameter  $z$ . The upper and lower curves correspond to  $\lambda = \log 5$  and  $\lambda = \log 10$ , respectively. The width (along the unstable manifold) of wavepacket  $|b\rangle$  is  $e^{\lambda(n+z)}$  times that of  $|a\rangle$ , where  $n$  is an integer. Numerical data for the ensemble of kicked-baker systems described in Section III C is plotted along with the theoretical curves from Eq. 45. As the stretching factor  $e^\lambda$  gets closer to unity, so does the correlation  $C_{ab}$ .

FIG. 2. The minimum correlation in the local densities of states  $C_{ab}$  for two wavepackets on an orbit of exponent  $\lambda$  is plotted versus the scarring IPR enhancement factor  $g(\lambda)$  for such an orbit. The theoretical curve is obtained from Eqs. 43, 45, while the data again comes from the ensemble of Section III C. The minimum inter-wavepacket correlation gets very close to unity for significant scarring enhancement factors  $g(\lambda)$ .

FIG. 3. Smoothed local densities of states are plotted for the universal hyperbolic test state  $|\Psi\rangle$  (higher peak) and a Gaussian wavepacket  $|a\rangle$  (lower peak), on a periodic orbit with exponent  $\lambda = |\log 0.18|$ . The system size is  $N = 800$ . Cut-off constant  $c = 0.6$  (see Eq. 24) is used to construct the state  $|\Psi\rangle$ . The theoretical curves (dashed) are obtained by fourier transforming the linearized autocorrelation functions of Eqs. 54, 6, respectively, while the data (solid curves) is obtained by ensemble averaging.

FIG. 4. In this figure, the inverse participation ratio (IPR) for hyperbolic test state  $|\Psi\rangle$  is plotted versus the log-time cutoff  $T_0$  (see Eqs. 51, 24), for various values of system size  $N$ . From bottom to top, the five curves correspond to  $N = 50, 100, 200, 400,$  and  $800$ . For each  $N$ , 26 points are plotted, for  $c = (1.1)^j$ ,  $j = -20 \dots +5$ . The orbit has exponent  $\lambda = |\log 0.18|$ , as in the previous figure. The upper dashed curve is the  $N \rightarrow \infty$  theoretical prediction (Eq. 57,  $F = 2$ ), which converges to the asymptotic prediction of Eq. 58 (lower dashed line) for large  $T_0$ . The linearized theory is expected to start breaking down for  $c \geq 1$  (rightmost six points on each data curve).

FIG. 5. This figure is a Husimi plot in phase space of the universal hyperbolic state  $|\Psi\rangle$  for log-time cutoff  $T \rightarrow \infty$  (i.e. the region plotted is well inside the linearizable region in classical phase space). The fixed point is at the center of the plot, and the horizontal and vertical axes correspond to the unstable and stable manifolds, respectively. The total area of the plot is  $12\sqrt{\hbar} \times 12\sqrt{\hbar}$ .

FIG. 6. Smoothed local densities of states are plotted for the off-resonance universal hyperbolic test state  $|\Psi\rangle$ , for off-resonance angle  $\theta$  ranging from 0 (tallest peak) in steps of  $\pi/10$  (to the left), through  $-2\pi$ , on a periodic orbit with exponent  $\lambda = |\log 0.18|$ . As in Fig. 3, the system size is  $N = 800$ , and the cut-off constant  $c$  is set to 0.6 (see Eq. 24). The data is obtained by ensemble averaging.

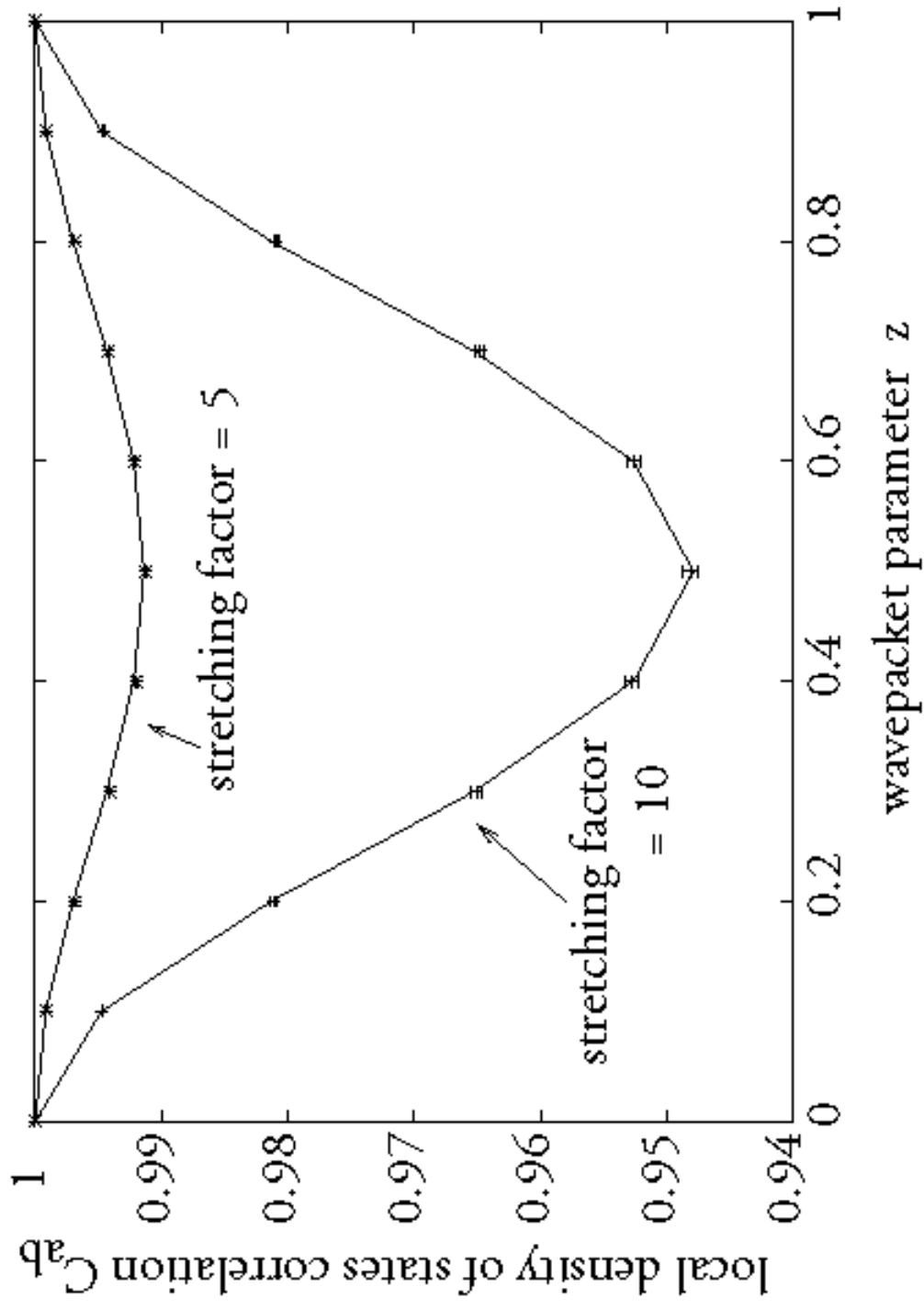
FIG. 7. Theoretically computed IPR values for the universal hyperbolic test states  $\Psi$  are plotted versus the log-time  $T_0$  for several values of off-resonance angle  $\theta$ . From top to bottom at  $T_0 = 1$ , the solid curves represent  $\theta = 0 \dots \pi$ , in steps of  $\pi/5$ . The dashed line is the limiting value for all of these at large  $T_0$  (Eq. 58). The single-Gaussian IPR (the  $T_0 \rightarrow 0$  limit) is 3.66 for this value of  $\lambda$ .

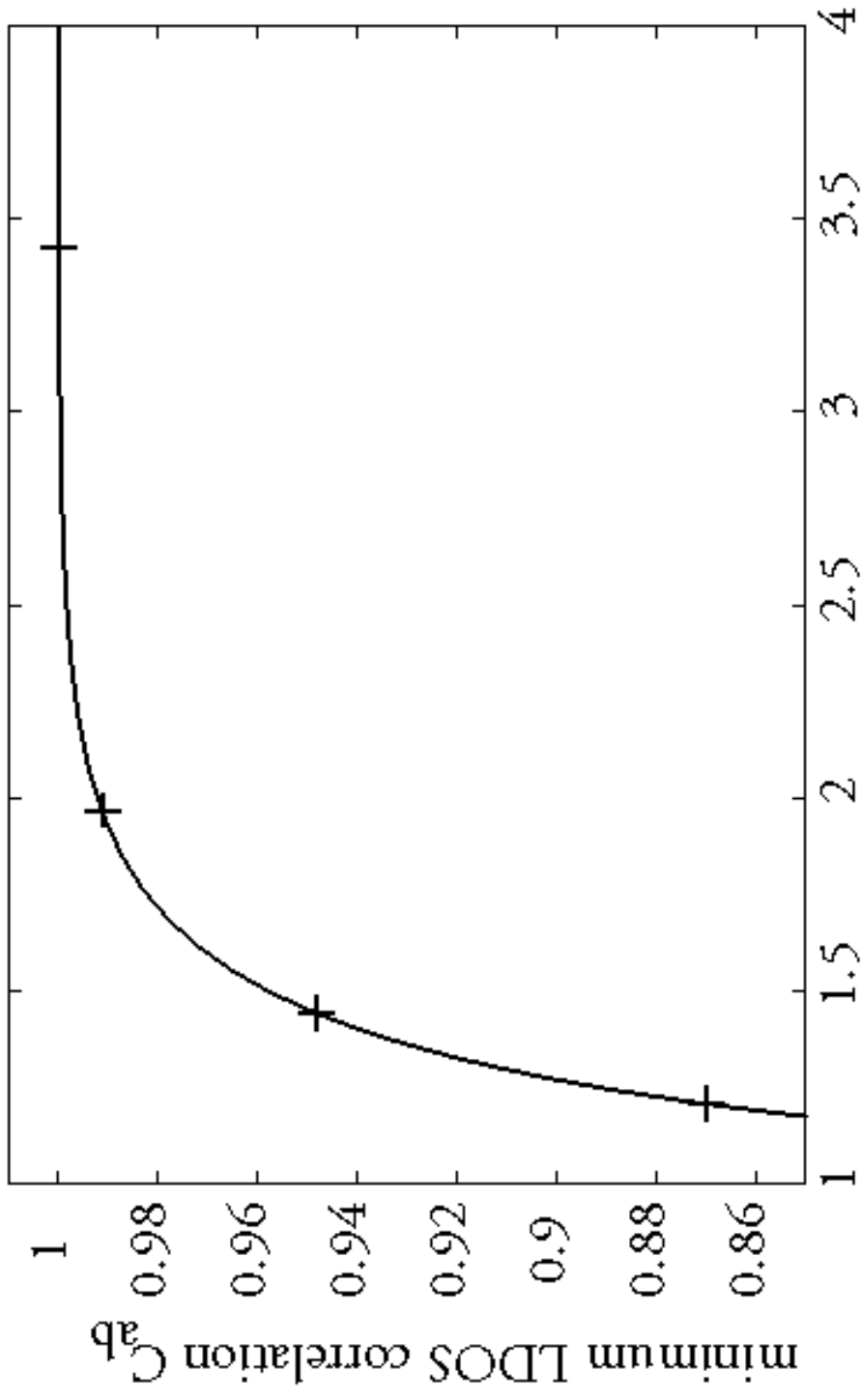
FIG. 8. The IPR is plotted here as a function of log-time  $T_0$ , as in Fig. 4, but for the off-resonance test state  $\Psi(\theta = \pi)$  of Eq. 61. Again, five data curves corresponding (bottom to top) to  $N = 50, N = 100, N = 200, N = 400,$  and  $N = 800$  are shown in the Figure, with cutoff parameter  $c$  varying from  $(1.1)^{-20}$  to  $(1.1)^{+5}$  from left to right within each curve. The stability exponent is  $\lambda = |\log 0.18|$ , as before. The upper dashed curve is the  $N \rightarrow \infty$  theoretical prediction obtained from Eqs. 57, 62. The lower dashed line is the asymptotic form of Eq. 58, to which the upper curve converges in the  $T_0 \rightarrow \infty$  limit. The linearized theory is again expected to break down for  $c \geq 1$  (the rightmost six points on each data curve).

FIG. 9. Here the IPR is plotted versus off-resonance angle  $\theta$ , for  $\lambda = |\log 0.18|$ ,  $N = 200$  and cutoff time parameter  $c = 0.6$ . The solid curve with errorbars represents ensemble-averaged data, while the dashed curve is the theory (Eqs. 57, 62). At small angles, the scarring strength is significantly above the single wavepacket IPR value of 3.5 (theoretical prediction: 3.66), while for larger angles we approach the ergodic RMT value of 2.

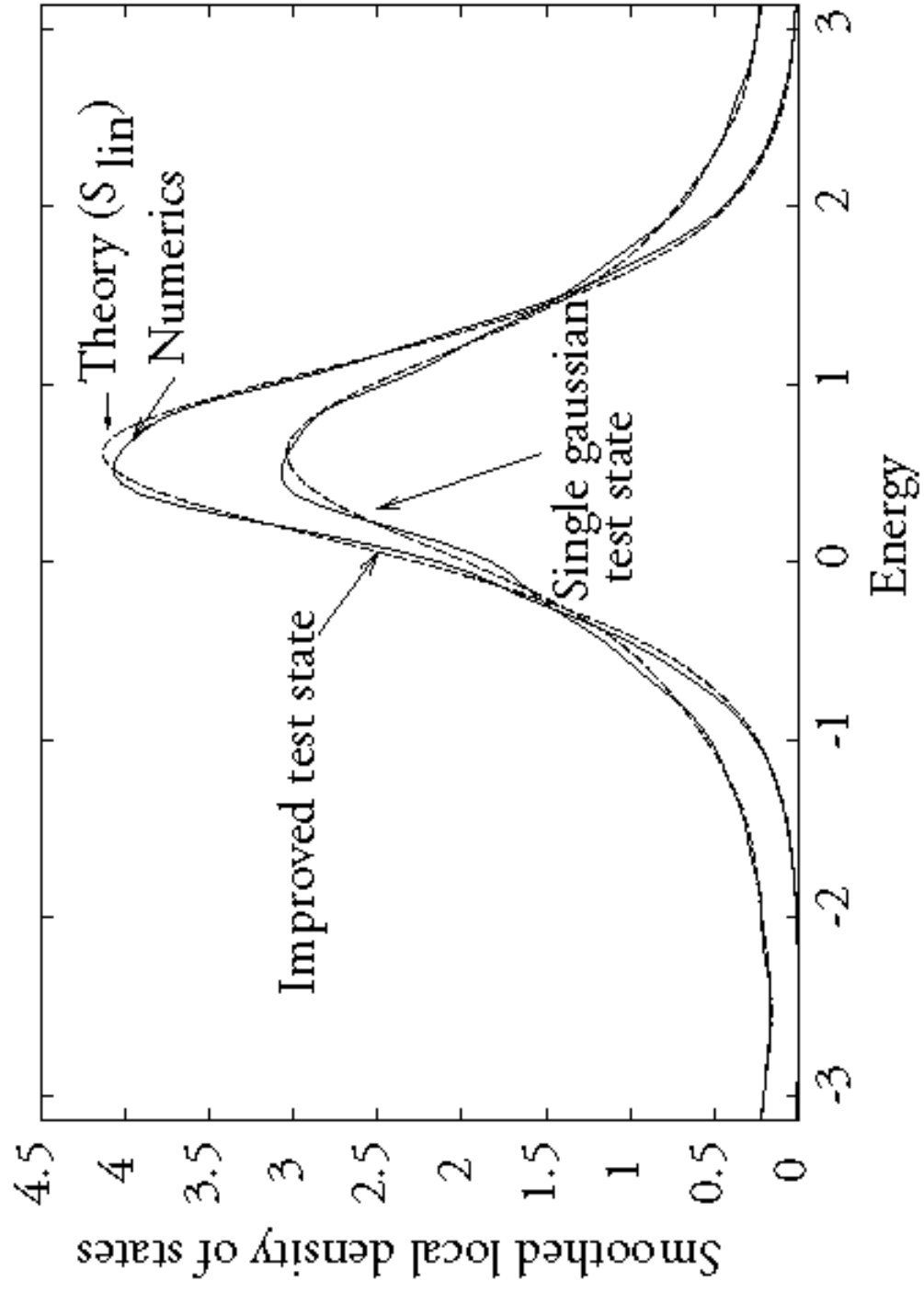
FIG. 10. Analogous to Fig. 5, this figure presents Husimi plots of the universal test state  $\Psi$  for off-resonance parameter values (a)  $\theta/\lambda = 0.8$  and (b)  $\theta/\lambda = 2.5$ . As before, the linearizable region is taken to be much larger than the displayed area of size  $12\sqrt{\hbar} \times 12\sqrt{\hbar}$ , centered on the periodic orbit.

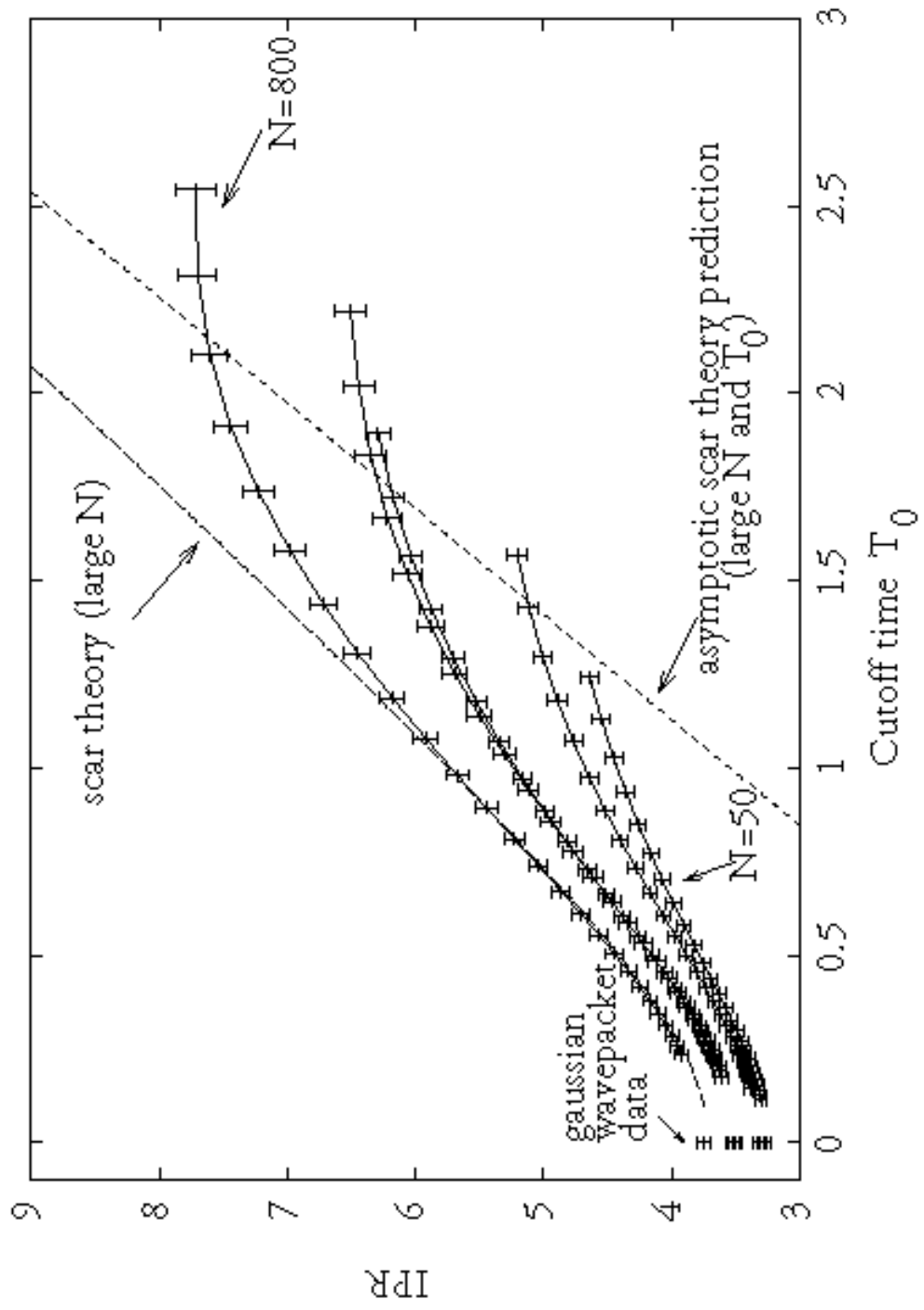
FIG. 11. Smoothed local densities of states are shown here for a Gaussian wavepacket placed on a period-2 orbit (double-peaked solid curve), and the universal test state  $\Psi$  constructed on the same orbit (tall single peak). The dashed curves represent theoretical predictions based on the linearized dynamics near the periodic orbit in question. The system is a kicked baker's map with kick potential acting on the middle strip (see Section VI C), and the periodic orbit has a total exponent  $\lambda = |\log 0.168|$  over the two-step period. One of two possible on-resonance energies has been chosen for the test state  $\Psi$ , which is again constructed using cutoff constant  $c = 0.6$  (as in the analogous calculation in Fig. 3 for a period-one orbit). The enhancement here is more dramatic due to the fact that universal scarring strength depends only on the exponent per unit time along the orbit, not on the orbit length itself.

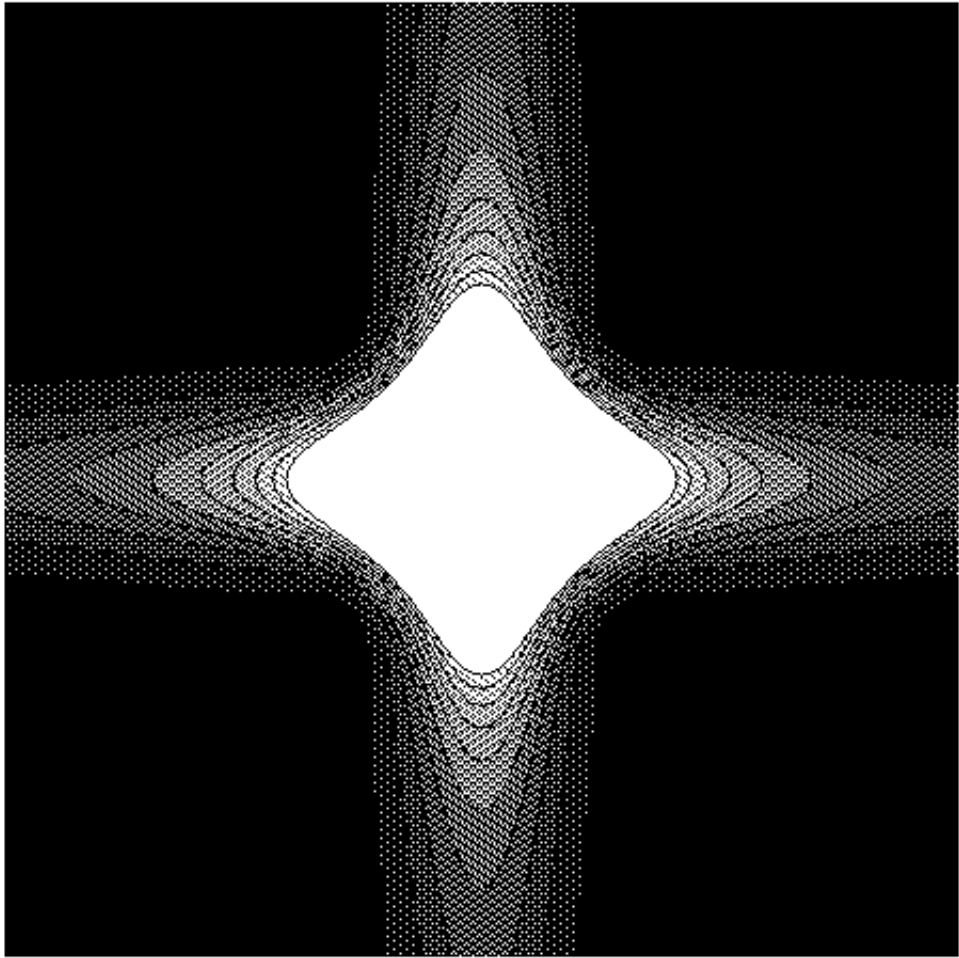


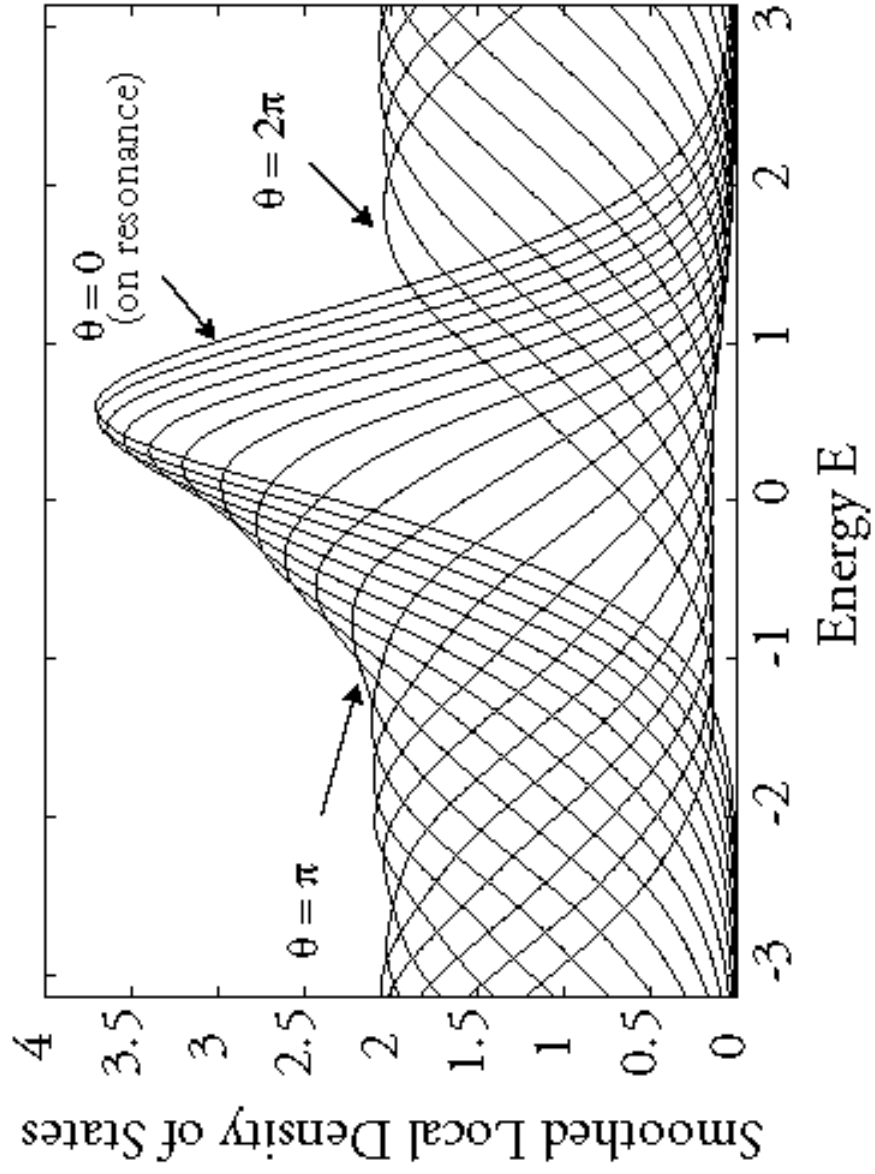


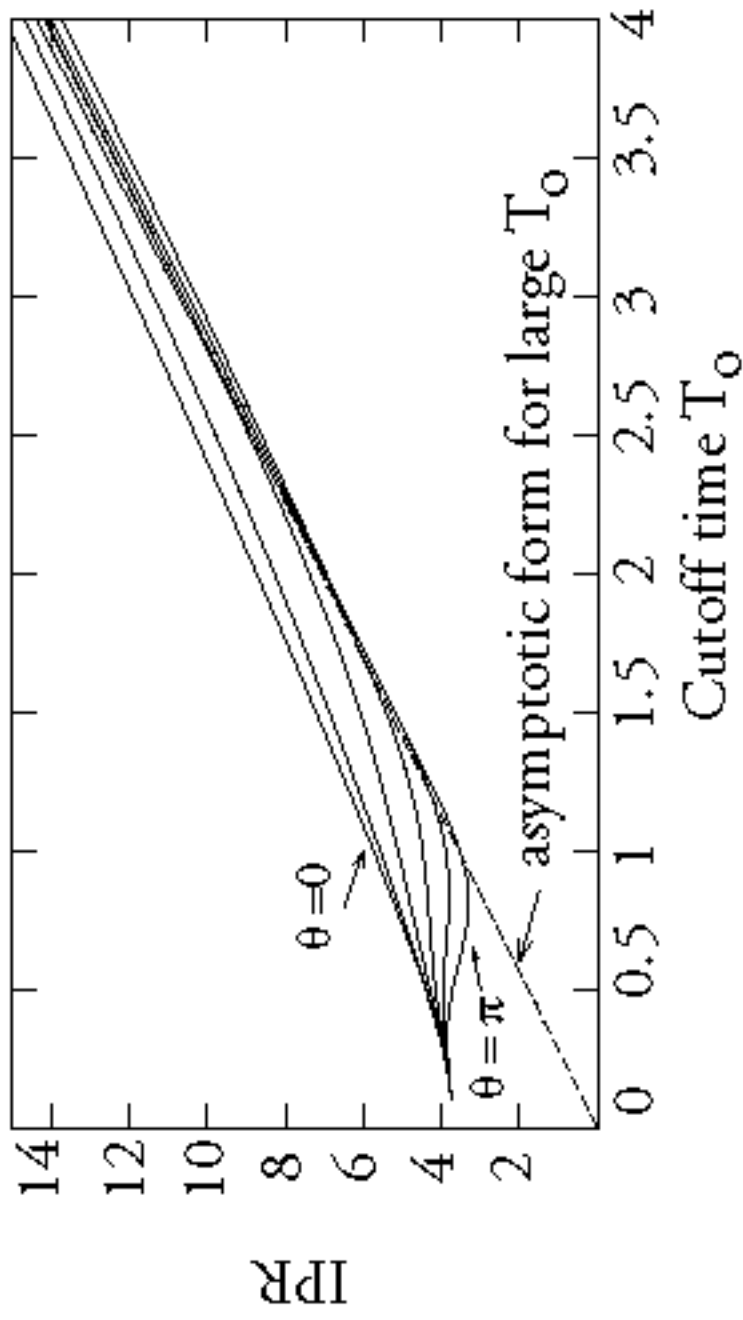
IPR enhancement factor  $g$  for wavepacket on orbit

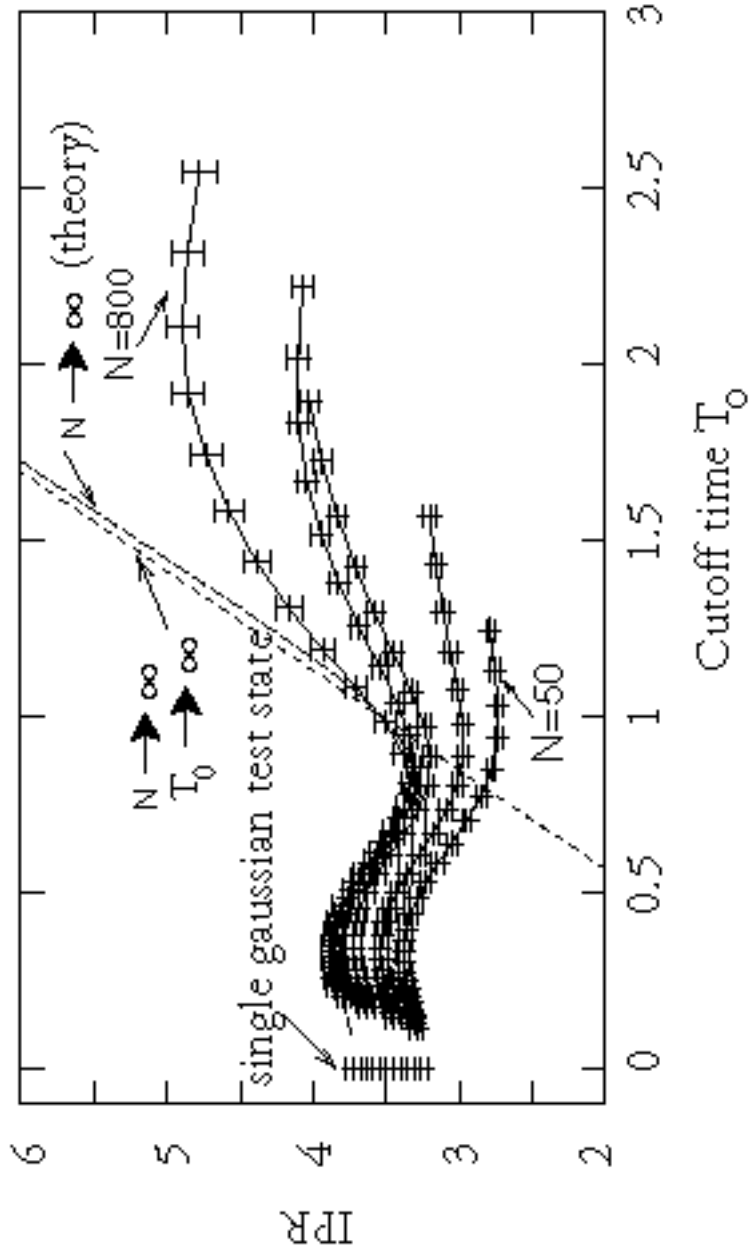


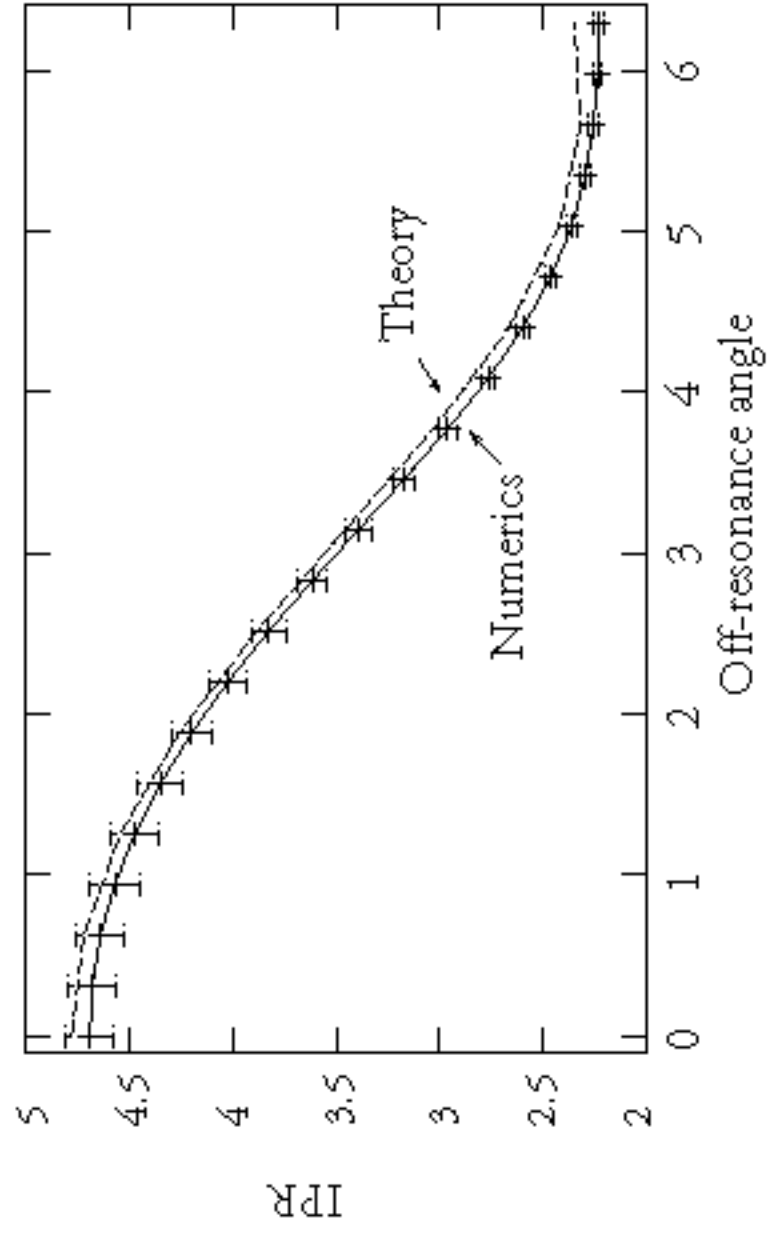


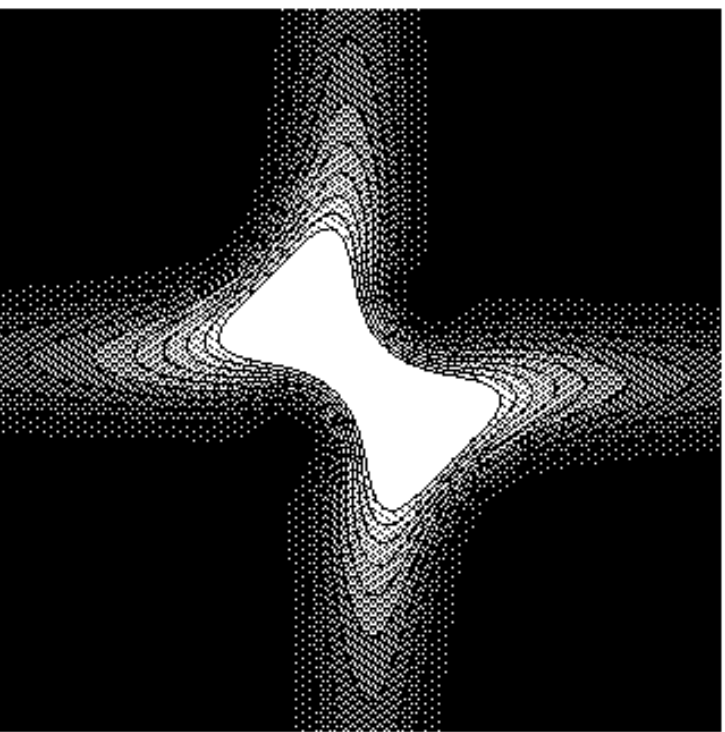




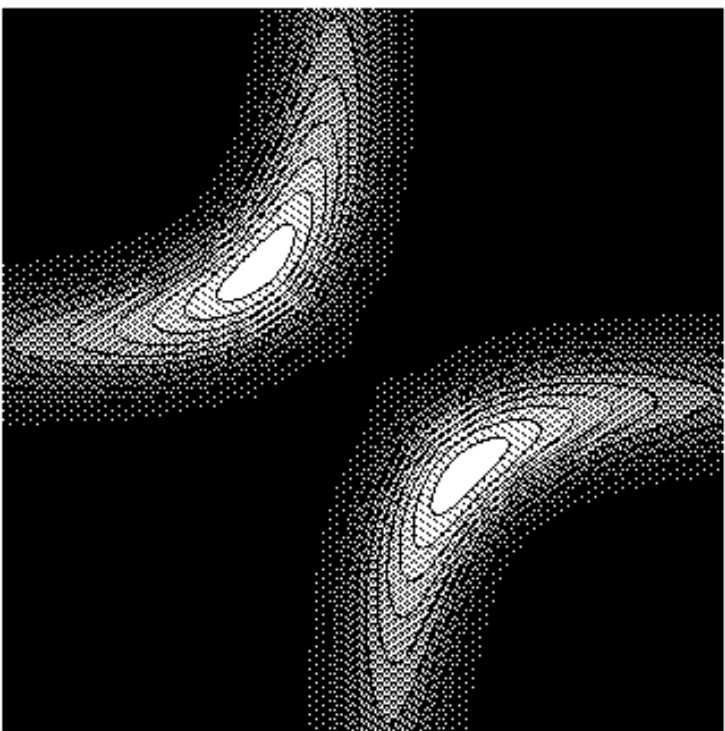








a



b

